Experimental study on dynamic stall of rigid and flexible hydrofoils in towing tank

Théo Simonet, Antoine Ducoin, Quentin Rakotomalala, Mathias Riou, Camille Yvin

Ocean Engineering 314 (2024) 119621

Contents lists available at ScienceDirect

Ocean Engineering

journal homepage: www.elsevier.com/locate/oceaneng

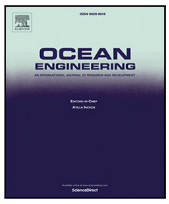

Research paper

Experimental study on dynamic stall of rigid and flexible hydrofoils in towing tank

Théo Simonet [a,*], Antoine Ducoin [a], Quentin Rakotomalala [b], Mathias Riou [b], Camille Yvin [c]

[a] Nantes Université, École Centrale Nantes, CNRS, LHEEA, UMR 6598, Nantes, France
[b] Centre d'Expertise des Structures et MAtériaux Navals (CESMAN) Naval Group, Bouguenais, France
[c] SIREHNA, Technocampus Ocean, 5 rue de l'Halbrane, 44340 Bouguenais, France

ARTICLE INFO

Keywords:
Dynamic stall
Composite hydrofoil
Optical fiber
Towing tank

ABSTRACT

This paper presents extensive results from a new experimental setup that operates in the towing tank at Centrale Nantes. The original feature of the setup is its capability to simultaneously induce inflow and dynamical pitching motions to large scale innovative appendages, and measure strains and hydrodynamic performances. The dynamic stall regimes of two hydrofoils are studied by means of the influence of the Reynolds number and the reduced frequency. The first appendage is a rigid rudder-like hydrofoil. The second one is a flexible composite hydrofoil equipped with optical fibers with arrays of fiber bragg gratings to measure local strains. The rudder-like hydrofoil performances behave non-linearly, which is the consequence of boundary layer detachments due to the hydrofoil's thickness and the large angles of attack tested. A significant quasi-static hysteresis effect was also observed on the lift due to stall. The composite hydrofoil shows a more linear behavior, with an earlier and sharper stall effect. The data demonstrated setup capabilities to capture subtle flow phenomena. Finally, as the lift coefficient and the strains are assessed with independent measurement systems, their close proximity demonstrates the good accuracy of the experimental setup and the link between lift and structural bending deformation.

1. Introduction

Within marine engineering, a growing interest surrounds the physics involved on innovative lifting appendages. The constant development of lifting devices such as flexible composite propeller blades or new shapes of ship rudders or hydrofoils bring new problematic in the area of Fluid–Structure Interaction (FSI) and 3D dynamic stall phenomena. This lack of knowledge primarily arises from the inherent difficulties to study such phenomena both experimentally and numerically. On one hand, high-fidelity CFD simulations such as LES (Large Eddy simulation) or DNS (Direct Numerical Simulation) allow precise descriptions of fluid flows (Visbal and Garmann, 2018; Shayanpoor et al., 2020), but the computational cost is still too expensive to study large ranges of parameters and/or complex geometries. On the other hand, current experimental facilities are mostly restricted to low Reynolds numbers, or appendages with small scales and/or low aspect ratios. Moreover, only few studies concern the interaction between static stall and the appendage flexibility, and these works are mostly restricted to experiments (Ducoin et al., 2012). In addition, we are not aware of any study about the interaction of the appendage flexibility and the dynamic stall phenomenon. Therefore, there is a need for large-scale experimental database, firstly to enhance the understanding of dynamic stall combined with fluid structure interaction, and then to provide test cases to validate numerical methods.

Experimental studies on dynamic stall

The static and dynamic stall phenomenon was subject to numerous researches in the last decades. The National Renewable Energy Lab. (NREL) published a series of comprehensive reports about static and dynamic stall regimes of various 2D airfoils, with Reynolds numbers up to $Re = 1\,500\,000$. For examples see Janiszewska et al. (1996), Ramsay et al. (1995), Hoffmann et al. (1996), Reuss Ramsay et al. (1996). Theses experiments were conducted in a wind tunnel at the Ohio state University. All data are available in open access on the NREL website. Nevertheless, there is not yet a consensus in the literature about the influence of the Reynolds number on the dynamic stall phenomenon. Some authors found that the Reynolds number play a minor role in dynamic stall (Zhang and Schlüter, 2012; Choudhuri and Knight, 1996; ROBINSON and WISSLER, 1988), while a recent high-fidelity study highlighted the sensitivity of the laminar separation bubble to Reynolds number (Benton and Visbal, 2019), see Choudhry et al. (2014), Gardner et al. (2023) for literature reviews. Additionally, Choudhry et al. (2014)

* Corresponding author.
E-mail address: theo.simonet@umontpellier.fr (T. Simonet).

https://doi.org/10.1016/j.oceaneng.2024.119621
Received 13 September 2024; Received in revised form 18 October 2024; Accepted 22 October 2024
Available online 12 November 2024

conjectured that the dynamic stall process is greatly influenced by the boundary layer regime prior to any unsteadiness. The maximal lift value increasing with the pitching reduced frequency has been widely reported in literature (Choudhry et al., 2014; Jumper et al., 1987; Gardner et al., 2023). This phenomenon is attributed to the detachment of the primary stall vortex, denoted as stall onset, that is delayed to a higher angle of attack when the reduced frequency increases. Mulleners and Raffel (2012) used time resolved Particle Image Velocimetry (PIV), with different coherent structure identification methods on a pitching airfoil. The approach enables a precise analysis of the flow field and led to a better understanding of the stall onset phenomenon at $Re = 900\,000$. The authors proposed a definition based on underlying physical mechanisms to differentiate deep and light dynamic stall. That is to say, light dynamic stall occurs when the angle of attack starts decreasing before the dynamic stall onset, while deep stall characteristics are observed otherwise (Mulleners and Raffel, 2012). Holst et al. (2019) conduct dynamic 2D experiments at Reynolds numbers up to $Re = 180\,000$. The setup in the wind tunnel permits a 180° rotation of the airfoil, enabling the study of numerous flow regimes experienced by vertical axis wind turbines. Andreu Angulo and Ansell (2019), with an open-return wind tunnel, studied the influence of aspect ratio on dynamic stall of 3D wings. The experimental setup allows to test wings with aspect ratios up to $AR = 5$ ($Re = 400\,000$). Le Fouest et al. (2021) studied the transition between dynamic stall and quasi-static stall (NACA0018, $Re = 75\,000$). The authors proposed a criterion on the motion of the profile to be called quasi-static. That is to say, in order to have negligible inertial lift contributions, the reduced pitch rate should be inferior to $\frac{c\dot{\alpha}}{2V} < 10^{-4}$, where c is the airfoil chord length, $\dot{\alpha}$ is the airfoil pitch rate, and V is the incoming flow speed. Ullah et al. (2024) studied the evolution of the flow structure and the surface pressure imprint of a finite pitching wing using Particle Image Velocimetry (PIV) and Pressure Sensitive Paint (PSP) techniques. The setup is able to capture spanwise variations of the dynamic stall vortex propagation toward the trailing edge. Moreover, the PSP results captured the tip unloading period during the pitching motion ($AR = 4$, $Re = 200\,000$). Bø ckmann and Steen (2014) and Bøckmann (2015) studied propulsive regimes of a 3D oscillating hydrofoil in a towing tank. The dynamic stall was induced by simple harmonic motions of the hydrofoil, and by combined pitching and heaving motions ($AR = 10$, $Re = 200\,000$). In addition, it is now established that dynamic stall process can vary significantly from cycle to cycle due to stochastic variations (Gardner et al., 2023). It has also been observed that variations can be clustered into distinct groups with clear fluctuations (Holst et al., 2019). For a broader overview of dynamic stall phenomenology, the reader can refer to the recent literature review of Gardner et al. (2023). The review cover dynamic stall experiments, from flight tests to pitching airfoils. It appears that very few experimental data are available on the dynamic stall of marine appendages at relatively large scale.

Numerical studies on dynamic stall

Karbasian and Kim (2016) studied the behavior of vortices during the dynamic stall of an oscillating pitching hydrofoil. The study showed that there are time delays between the maximum circulation of main vortices and corresponding peak of the lift coefficient. Amini et al. (2019) performed dynamic stall simulations of a pitching hydrofoil near a free surface. It was found that both submergence depth and frequency of rotation significantly affect lift and drag coefficients. Hammer et al. (2022) performed wall-resolved large-eddy simulations (LES) to study the aspect ratio influence on the dynamic stall process of a finite wing. The results showed an increase in lift slope, average loads, peak loads, and earlier stall with aspect ratio ($AR = 4, 8$ and 16, $Re = 200\,000$). Recently, Khalifa et al. (2023) showed that dynamic stall is intrinsically a three-dimensional phenomenon. The authors used multiple detached eddy simulations (DES) for two- and three-dimensional simulations, and compared the results against experimental measurements from the literature. The study showed that three-dimensional simulations surpass two-dimensional ones in capturing the stages of dynamic stall and in predicting the lift coefficient values ($Re = 135\,000$).

Experimental studies on fluid–structure interaction of lifting devices

Interest in fluid–structure interaction for marine application has been stimulated by the development of composite profiles, which aim to passively control deformations to enhance performances. Studies on the topic often combine numerical and experimental methods. Akcabay et al. (2014) compares experiments in cavitation tunnel with RANS simulations (two degrees of freedom system), to study the influence of cavity-induced vibrations on a static NACA66 hydrofoil, below critical angle of attack (2D, $Re = 750\,000$). The cavitation dynamics and its influence on hydrofoil's deformation were highlighted. Zarruk et al. (2014) studied hydroelastic performance of composite trapezoidal hydrofoils in static condition beyond stall in a water tunnel ($AR = 3.33$, $Re = 1\,000\,000$). They measured the forces, moments and tip deflection. Young et al. (2018) conduct a study about bend–twist coupling effects on the steady-state hydroelastic response of composite hydrofoils, below and above stall incidence ($AR = 3.33$, $Re = 1\,200\,000$). The authors used high-speed images processing to measure deflections of the hydrofoil. In the same water tunnel facility, Herath et al. (2021) characterized the hydrodynamic response of an optimized passive shape-adaptable composite hydrofoil. FSI simulations were performed to comfort the findings. Numerical results were observed to closely match the experimental hydrodynamic results and structural deformations. The study highlighted the better performances of the optimized hydrofoil, compared to the other ones ($AR = 3.33$, Re up to $1\,000\,000$). Pernod et al. (2019) investigate the hydroelastic response of a composite hydrofoil below and above stall incidence. Hydrofoil strains were measured by a fully-distributed-optical fiber sensor within the composite plies. Good correlation was achieved with a tightly coupled high-fidelity fluid–structure interaction numerical model ($AR = 2.13$, $Re = 540\,000$). In the context of bio-mimetic propulsion, Bi and Cai (2012) conducted experiments in a water tank to investigate the influence of spanwise flexibility of hydrofoils. Hydrofoils were subjected to a rolling motion, in order to mimic fish pectoral fins ($AR = 2$, $Re = 20\,000$). In the same context of bio-mimetic propulsion, Heathcote et al. (2008) and also Cleaver et al. (2016) studied the influence of spanwise flexibility of heaving hydrofoils ($AR = 1.5 - 3$, $Re = 10\,000 - 30\,000$). Heathcote et al. (2008) used a high-speed video camera and a motion-tracking software to measure the hydrofoils deformation. This experiment became a notable benchmark for numerical methods validation, either for full FSI methods (Gordnier et al., 2013; Cho et al., 2019), or methods with imposed deformations of the hydrofoil (Faure et al., 2022; Simonet et al., 2020). The correspondence between experimental and numerical results is mainly well established. The exception is for the most flexible hydrofoil, for which the trust coefficient exhibits high frequency oscillations that are not fully understood. Recently, Young et al. (2023) conduct experiments in the large depressurized wave basin at MARIN (Netherlands), to study hydrodynamics of a flexible surface-piercing hydrofoil in waves. The experimental setup enabled the investigation of the effect of waves and ventilation on structural dynamics. Perali et al. (2024) investigated numerically and experimentally the hydroelastic response of a flexible hydrofoil (NACA0015) under both wetted and cavitating flow conditions. Numerical simulations were performed using a fully implicit coupling between a Reynolds-averaged Navier–Stokes (RANS) solver (ISIS-CFD solver) and a modal approach for the structure. For wetted flow conditions, numerical results show a good agreement with the experiments, for both rigid and flexible hydrofoils. For cavitating flows, amplitudes of vibrations are well predicted by the computations. However, experiments with small cavitation numbers exhibit a frequency lock-in that was not captured by the numerical approach.

Fiber bragg grating for strain measurement

The utilization of Fiber Bragg Gratings (FBG) has shown very promising results in obtaining precise measurements of both static and

dynamic structural strains (Ducoin et al., 2023; Seaver et al., 2006; Phillips et al., 2017). Optical fibers with arrays of FBG are lightweight, small in size and insensitive to corrosion. It can be embedded in the composite appendage during the manufacturing process (Seaver et al., 2006; Ducoin et al., 2023), or glued to the surface after manufacturing (Phillips et al., 2017). Embedded FBG has also been used to detect and characterize composite damage, due to delamination (Cook et al., 2017), and from impacts (Yeager et al., 2017). Recently, (Ducoin et al., 2023) conducted steady and unsteady measurements on a composite propeller blade in the towing tank at Centrale Nantes, France. Optical fibers with arrays of FBG were embedded in both pressure and suction sides of the blade. Forces, moments and strains were measured simultaneously. Flow detachments were identified with Strouhal frequencies observed on the signals and appears to interacts with the structural strains. This setup presented some limitations as it was limited to static condition, and as the frame was subjected to large level of vibration from the towing tank.

In this paper, extensive results from a new experimental setup in the towing tank of Centrale Nantes, France are presented. The objective of this paper is to present extensive results from a new experimental setup in the towing tank of Centrale Nantes, France. The concept was design to overall improve the capability of the previous setup presented in Ducoin et al. (2023). The original feature of the setup is its capability to simultaneously induce dynamical pitching motions to the appendages, and measure strains and hydrodynamic performances. It has been designed to study hydrodynamics of large scale innovative appendages (span $\times$ chord $\approx$ 1 $\times$ 0.5 m, $Re \approx 1\,000\,000$). The fully submerged appendages can be dynamically pitched with an amplitude $\alpha_{max} = \pm 45°$. The system is equipped to receive and process signals of optical fibers with arrays of FBG for strain measurements. The tests have been carried out to investigate the influence of the Reynolds number, and the reduced frequency, on hydrodynamics of two different pitching appendages in dynamic stall regimes. Reynolds numbers up to 1 000 000, and reduced frequency $k = \pi f c/V$ up to 0.14 are considered. Tabulated data with uncertainties of all figures presented in the Results section are available as supplementary material associated with the article.

2. Materials and methods

2.1. Experimental setup

The towing tank at Centrale Nantes is 140 m long, by 5 m wide, with a constant depth of 3 m. The tank carriage has a maximum velocity of 8 m·s^{-1}. The original experimental setup is installed on a dedicated and effectively rigid metal frame fixed to the carriage, see Fig. 1(a). A rotating motion is generated along the horizontal direction with a AKM2G-41XLANCN2-0V servo motor from Kollmorgen, which is coupled with a reduction gearbox. The motion is redirected by an angle drive to get the desired pitching motion in the vertical direction, see Fig. 1(a). A FX2.6 6-components hydrodynamic balance, manufactured by Sixaxes, transmits the motion to a clamping mechanism designed to accommodate various types of appendages, see Fig. 1(b). A flat-bottomed hull is fixed to the frame to limit free surface effects, see Fig. 1(c). The hull is made of wood and is 5 m long, 0.5 m wide, and 0.6 m high. A reaming has been realized in the bottom of the hull to allow the clamping mechanism to pass through. The full experimental setup is represented in Fig. 2.

The hydrodynamic balance measures forces ($F_{\tilde{x}}$, $F_{\tilde{y}}$, $F_{\tilde{z}}$), and moments ($M_{\tilde{x}}$, $M_{\tilde{y}}$, $M_{\tilde{z}}$), in the appendage coordinate system, located near its root, where the $\tilde{x}$-axis is in the chordwise direction, the $\tilde{z}$-axis is in the spanwise direction, i.e. the vertical direction, and the $\tilde{y}$-axis completes the orthonormal trihedron. The hydrodynamic coefficients can then be computed by projection of the loading into the carriage coordinate system, see Fig. 2. The sampling rate of the hydrodynamic balance is 1000 Hz. The maximum forces and moments, and the corresponding maximal uncertainties are listed in the Table 1.

Table 1
Hydrodynamic balance specifications.

	$F_{\tilde{x}}$	$F_{\tilde{y}}$	$F_{\tilde{z}}$	
Max. loading	400	2 000	2 000	N
Max. uncertainty	± 5.61	± 6.32	± 4.11	N
	$M_{\tilde{x}}$	$M_{\tilde{y}}$	$M_{\tilde{z}}$	
Max. loading	1 200	240	100	N · m
Max. uncertainty	± 2.47	± 0.62	± 0.61	N · m

Table 2
Homogenized material properties of the composite flexible hydrofoil (orders of magnitude).

Elastic modulus	Shear modulus	Poison's ratio
$E_{\tilde{x}} \approx 60$ GPa $E_{\tilde{y}} \approx 20$ GPa	$G_{\tilde{x}\tilde{y}} \approx 20$ GPa	$\nu_{\tilde{x}\tilde{y}} \approx 0.7$

The servo motor allows the angle of attack of the appendage to dynamically vary from −45° to 45°. The servo motor has a 2048-line encoder, i.e. it has 2048 A signals per revolution, and 2048 B signals per revolution (offset by 90°). The drive interprets each rising edge and falling edge of A and B signals, resulting in 8192 angular positions per revolution. At the output of the 1/70 reduction gearbox, the theoretical precision on the angle of attack given to the appendage is therefore 6.3×10^{-4} degree. The torsional flexibility of the mechanical components linking the angle drive to the appendage, see Fig. 1(b), leads to an offset angle of attack below 10^{-2} degree, when the maximal torque admitted by the hydrodynamic balance is applied. During all dynamical tests considered in this study, the following error of the servo motor never exceeded 0.15°.

2.2. Rigid and flexible appendages

In the present work, hydrodynamics performances of two appendages are investigated. The first appendage has a geometry similar to ship rudders. It is a thick, rigid, rectangular hydrofoil made of aluminum, see Fig. 3(a). The cross section is the NACA0020, the span is 1 m and the aspect ratio is $AR = 2$. The pitching motion is applied at the quarter chord of the hydrofoil, i.e. at aerodynamic center. The hydrofoil surface roughness is significant, and is likely to promote turbulent flow. It has to be noted that during the experimental campaign, the hydrofoil surface was regularly cleaned to remove alumina deposits formed by corrosion. In the rest of the article, this rudder-like hydrofoil will be referred to as the rigid hydrofoil.

The second appendage has been designed to be representative of a simplified flexible propeller blade. This appendage has already been used in Rakotomalala et al. (2024) for numerical vibration sound analysis. It is a thin, flexible, trapezoidal hydrofoil with a straight trailing edge. The cross section is the NACA0006, the span is also 1 m and the taper ratio and aspect ratio are respectively $TR = 0.3$ and $AR = 6.15$, see Fig. 3(b). The pitching motion is applied at the mid-chord of the hydrofoil's root. In the rest of the article, this simplified propeller blade will be referred as the flexible hydrofoil. It was manufactured using prepreg carbon fiber reinforced epoxy, alternating between unidirectional and fabric layers. The hydrofoil section is mainly composed of unidirectional plies oriented at 0°, in fact the unidirectional plies are stacked by 4th and are followed on either side by only one fabric ply oriented at 45°. This sequence is repeated until a maximum of 26 plies is reached at the root of the foil. The orders of magnitude of the main homogenized material properties are shown in Table 2. The rigid and flexible hydrofoils were initially chosen for unrelated studies, their respective results will be presented but are not intended to be compared.

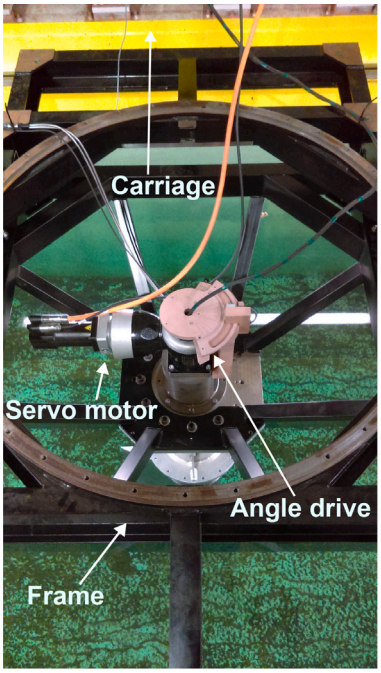

(a) Top view of the experimental setup, without hull.

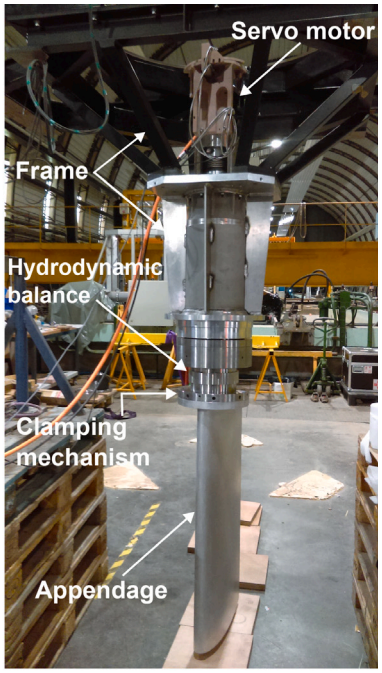

(b) Out of water experimental setup, without hull.

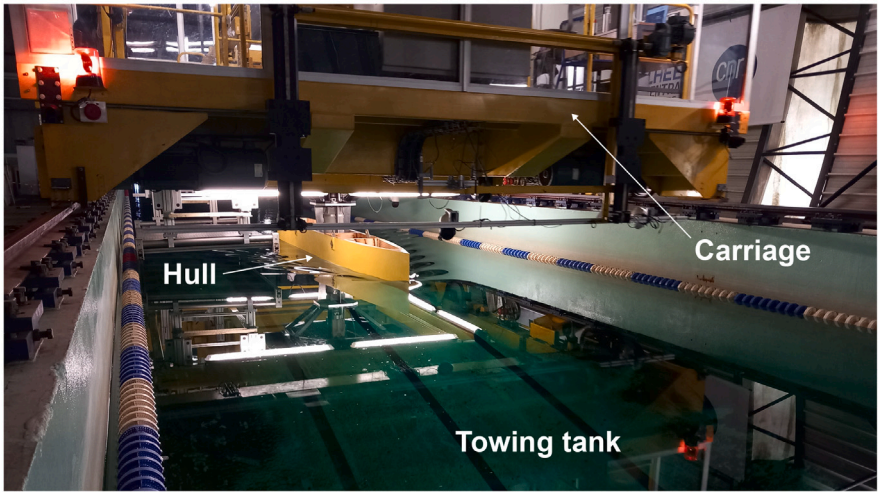

(c) Towing tank with the experimental setup.

Fig. 1. Experimental setup.

In order to measure hydrofoil's strains, two optical fibers with arrays of fiber bragg gratings have been glued on the surface of the flexible hydrofoil. A total of 16 FBG sensors are distributed over the hydrofoil surface, see Fig. 4. 15 sensors are oriented in the spanwise direction and one in the chordwise direction, in order to get insight about spanwise and chordwise deflection respectively. The strains measured with the optical fibers are obtained with a FS22DI interrogator from HBM. The interrogator has a sampling frequency of 1000 Hz, with a wavelength measurement ranging from 1500 nm to 1600 nm. The systematic uncertainty of the strain measurements has been quantified by comparison with strain gauges on another setup. The measurements showed a strain deviation lower than 3%.

Regarding the strains presented in the Results section, the main focus is on the sensor denoted ε_1, see Fig. 4. This sensor is located close to the hydrofoil root and leads to the largest strain signals. Sensors denoted ε_2 to ε_5 are also considered to give insight about the spacial distribution of strains. These five sensors are oriented in the spanwise direction, the Table 3 gives their spacial coordinates on the hydrofoil's surface. These sensors were chosen for their roughly similar position in the chordwise direction, in order to isolate the effect of the spanwise position. The full strain field will be analyzed in detail in future studies.

Table 3
Coordinates of the main FBG sensors on the hydrofoil's surface (expressed in the appendage coordinate system where the origin is at the leading edge of the root section).

	$\tilde{x}$	$\tilde{y}$	$\tilde{z}$	
ε_1	97	0	75	mm
ε_2	156	0	88	mm
ε_3	149	0	273	mm
ε_4	166	0	587	mm
ε_5	144	0	740	mm

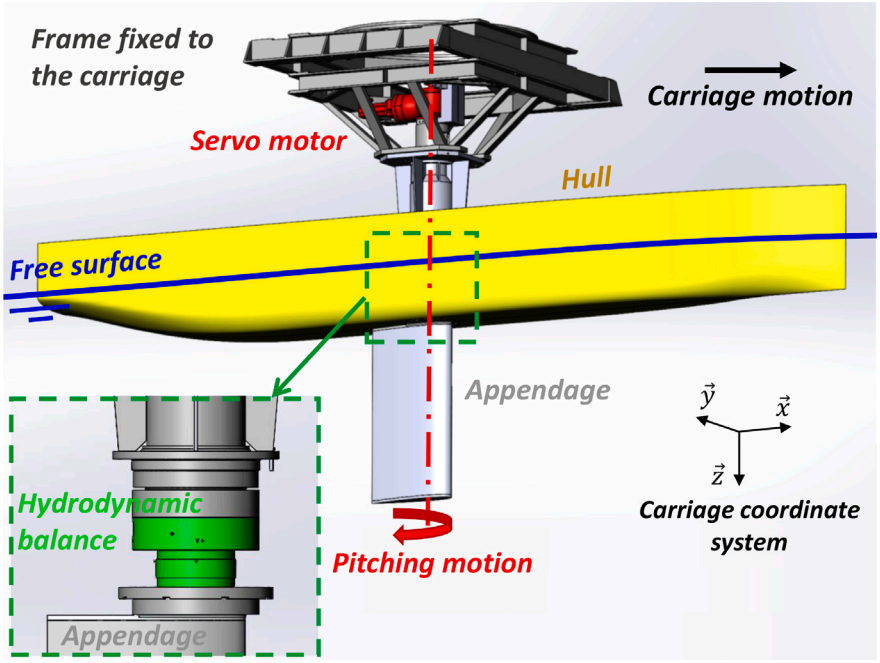

Fig. 2. Full experimental setup representation.

(a) Aluminium rigid hydrofoil.

(b) Composite flexible hydrofoil.

Fig. 3. Rigid and flexible appendages.

2.3. Setup characterization

2.3.1. Vibration analysis

Vibration analysis were conducted in the towing tank in order to depict the dynamic excitation originating from the experimental setup itself. An accelerometer was fixed on the clamping mechanism to measure vibrations at the appendage root, see Fig. 1(b). Fig. 5(a) shows the signals spectra after stimulation of various part of the setup. The Clamping mechanism, the lower part of the setup frame and the carriage super-structure were stimulated by a hammer blow. Spectra are normalized for readability. The clamping mechanism and the setup frame show clear main natural frequencies around 115 Hz and 205 Hz respectively, while the carriage super-structure exhibits a range of lower frequencies below 50 Hz.

Fig. 5(b) shows the lift spectra taken from the force measured by the hydrodynamic balance. It is obtained from tests with the rigid hydrofoil at a constant pitch angle of 25°, and various constant carriage speeds. Spectra are normalized and shifted for readability. Three vibration components have been identified. The lower frequency corresponds to the rail plates, which is proportional to the carriage velocity ($V/f \approx 0.72$ m). It have already been observed in previous studies using the towing tank at Central Nantes (Ducoin et al., 2023; Kerdraon et al., 2021). It is significantly reduced as compared to the previous studies, due to the high rigidity of the fixation model frame. The second and third main vibration components have a constant frequency of 5.1 Hz and 7.6 Hz respectively. This components are attributed to the carriage super-structure vibration, and they can be observed regardless of the carriage speed and the pitching actuation of the appendage. The lower frequencies observed can be associated to a combination of shed vortices frequencies and differences in the planarity along the towing tank rail. However, the letter are too close to the frequency range of interest to be filtered out.

2.3.2. Influence of the hull

The hull is used to fully submerge the appendage, and thus reduce free surface effects. In order to get insight of the hull influence on the measured data, tests were performed without hull. When the hull is not used, the setup is vertically positioned so that the upper surface of the appendage barely protruded above the free surface, see Fig. 6(a). Fig. 7 shows the lift coefficients obtained for the rigid hydrofoil, with and without hull, at Reynolds numbers $Re = 500\,000$ and $Re = 1\,000\,000$. Static values correspond to averaged values during runs with fixed pitch angles. Quasi-static values correspond to temporal values of dynamic runs with the lower oscillating frequency permitted by the tank length (i.e. $k = \pi f c/V = 0.008$). As expected, the lift coefficients obtained without hull appear underestimated compared to results with hull, for both Reynolds numbers. Figs. 6(b) and 6(c) show the flow around the barely surface-piercing hydrofoil during dynamic tests. No visualization have been performed during the corresponding static tests, but the free surface is believed to behave globally similarly. When the hull

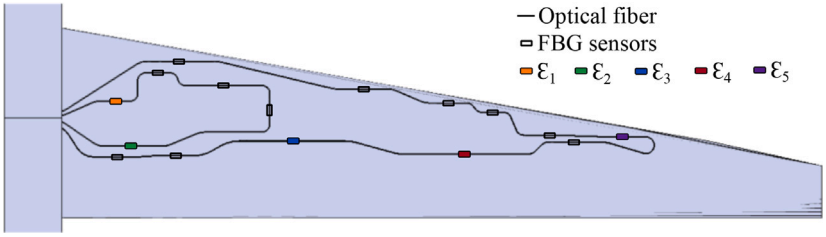

Fig. 4. Flexible hydrofoil surface with arrays of fiber bragg gratings.

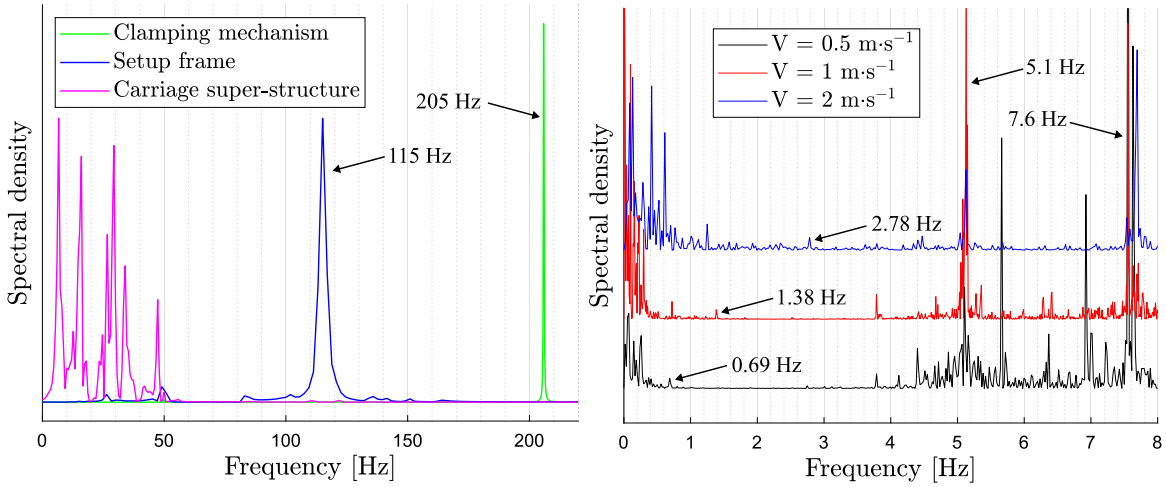

(a) Comparison of appendage root vibrations from stimulation of various part of the setup.

(b) Comparison of lift spectra obtained from tests with constant pitch angle of the rigid hydrofoil.

Fig. 5. Vibration analysis of the experimental setup.

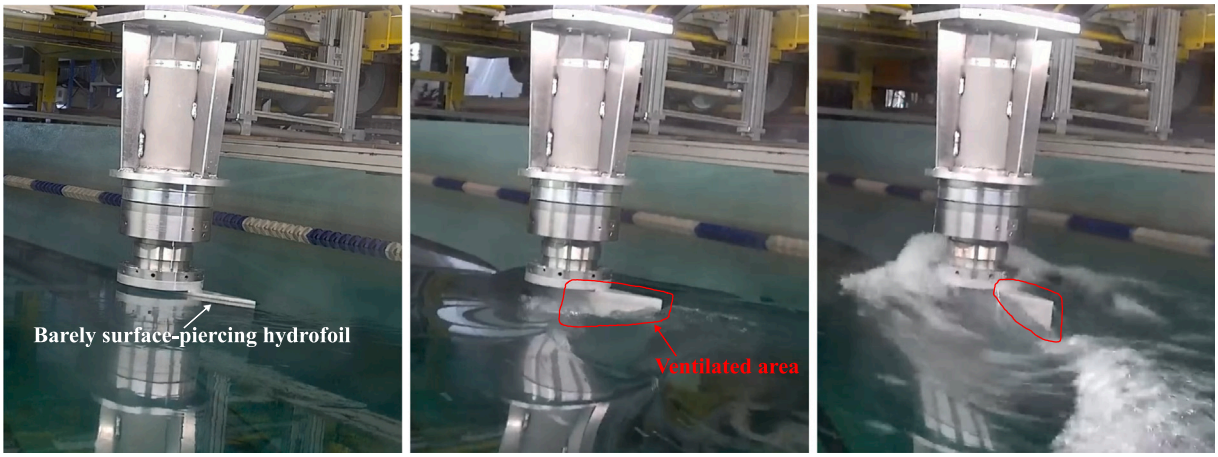

(a) Resting configuration.

(b) Moving configuration, $Re = 500\,000$.

(c) Moving configuration, $Re = 1\,000\,00$.

Fig. 6. Experimental setup without hull.

is not used, the underestimation of the lift coefficient comes from the free surface development, due to ventilation at the hydrofoil's surface, reducing the wetted area on the suction side of the appendage and thus reducing the lift, as studied by Harwood et al. (2014). Ventilation is mainly due to negative pressure produced at the suction side, which generates air suction at the hydrofoil's surface. This lift reduction appears slightly less pronounced for Reynolds number $Re = 1\,000\,000$, see Fig. 7.

Fig. 8 compares temporal lift coefficients evolution of static tests performed with and without hull. It covers a duration of 22 convective times $t_c = \frac{c}{V}$. The filtered signals come from a linear regression of the raw signals over a moving time window spanning two convective times t_c. The hull leads to a mostly constant lift coefficient, while the result without the hull is significantly fluctuating. It shows that the hull suppress effectively the free surface effect and stabilize the flow around the hydrofoil's root. The vibrations of the carriage super-structure are observable on the raw lift signals.

The hull prevent major free surface effects on the appendage, however it still have a minor variation around the hull both sides. Fig. 9 shows the bow wave formed around the hull for various carriage speeds. At $0.5\,\mathrm{m{\cdot}s^{-1}}$, the free surface remain flat around the hull. The bow wave then grows with the carriage speed up to $4\,\mathrm{m{\cdot}s^{-1}}$ where the

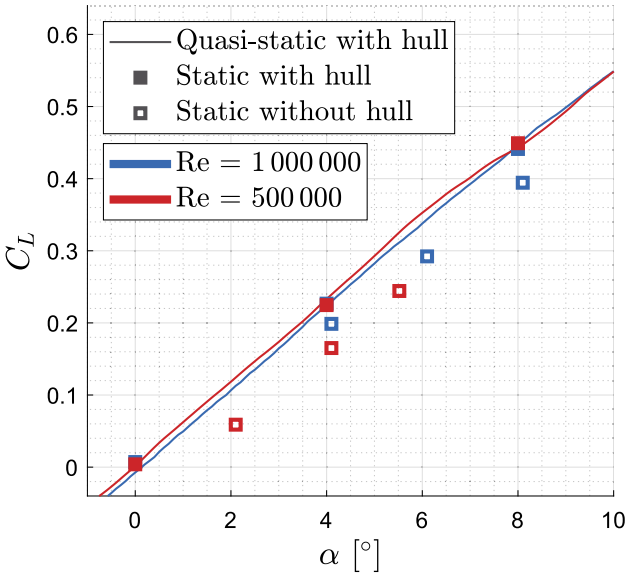

Fig. 7. Hull influence on the lift coefficient.

bow wave almost reach the top of the hull. Therefore, the setup limits the carriage speed to $4\,\mathrm{m{\cdot}s^{-1}}$ in order to prevent water entering the hull.

In the results section, lift and moment coefficients for rigid and flexible hydrofoils are presented, along with strain signals for the flexible hydrofoil. The drag coefficient remains to be characterized and is not presented in this paper.

2.4. Towing tank testing procedure

The experimental campaign was carried out during March and April 2023. Static, quasi-static, and dynamic tests were conducted. For static tests, the angle of attack of the hydrofoil was kept constant during the run. For dynamic tests, the hydrofoils was harmonically pitched with a zero average angle of attack: $\alpha(t) = \alpha_0 \sin(2\pi f t)$, where $\alpha(t)$ is the dynamic angle of attack, α_0 is the pitching amplitude, and f is the oscillating frequency. The pitching amplitudes for rigid and flexible hydrofoils are respectively $\alpha_0 = 25°$ and $\alpha_0 = 15°$ for the whole study. These values are chosen to encompass static stall angles of each profiles (NACA0020 and NACA0006 respectively). Reduced frequencies up to $k = \pi f \bar{c}/V = 0.14$ were considered. Where V is the carriage speed, and $\bar{c}$ is the mean chord length. Quasi-static tests correspond to dynamic test with the lowest reduced frequency permitted by the tank length, i.e. $k = 0.008$ for the rigid hydrofoil. The tests were performed at velocities ranging from $0.5\,\mathrm{m{\cdot}s^{-1}}$ to $4\,\mathrm{m{\cdot}s^{-1}}$, leading to chord based Reynolds numbers $Re = 160\,000$ to $Re = 1\,000\,000$. Considering that there is no incoming turbulence intensity in the towing tank, there could be likely some transitional regimes, in particular for the lower Reynolds number and low angles of attacks.

To compute the hydrodynamic coefficients and the Reynolds number involved, the water density and its dynamic viscosity were assumed to be $\rho = 1000\,\mathrm{kg{\cdot}m^{-3}}$ and $\mu = 10^{-3}\,\mathrm{Pa{\cdot}s}$ respectively. The angle of attack corresponding to $\alpha = 0°$ was defined by the configuration leading to zero lift through static runs. Due to the acceleration and deceleration phases of the carriage, the measurement windows of the runs varied slightly around 80 m to 105 m depending on the carriage velocity. The tank was allowed to settle for about 10 min between each run in order to avoid large-scale vortices induced by the previous run. Each test was repeated between one and four times depending on the test. The Tables 4 and 5 show the numbers of repetitions of each quasi-static and dynamic tests realized for the rigid and flexible hydrofoils respectively. The four test repetitions for quasi-static cases with the rigid hydrofoil

Table 4
Number of repetitions for quasi-static and dynamic tests (Rigid hydrofoil).

k \ Re	250K	500K	1M
0.008	4	4	4
0.025	1	2	2
0.05	1	2	2
0.08	1	2	2
0.14	1	2	2

Table 5
Number of repetitions for dynamic tests (flexible hydrofoil).

k \ Re	160K	330K	490K
0.0085	2	1	1
0.017	2	2	2
0.034	2	2	2
0.05	2	2	2
0.1	2	2	2

are composed of two runs with positive angles of attack, and two runs with negatives angle of attack. For the static tests, 3 repetitions were realized for each angle of attack considered with the flexible hydrofoil. With the rigid hydrofoil, between 2 and 4 tests repetitions were realized depending on the angle of attack.

Fig. 10 shows some selected row temporal signals taken simultaneously during an entire towing tank test. The measurement starts when the carriage procedure has been sent to the trigger. The later send a 5 V voltage (see $t \approx 5$ s) to synchronize the carriage velocity V, dynamic angle of attack α given by the motor, forces and moments from hydrodynamic balance and strain signals for the composite hydrofoil. In the first stage of the procedure, the towing tank is lift down with hydraulic piston so that the wheels are in contact with the rails, which generates an overshoot at $t \approx 12$ s on the physical signals (see for instance M_z). Then the hydrofoil pitching oscillation $\alpha(t)$ starts, followed by the carriage acceleration. On Fig. 10, constant velocity is reached around $t \approx 25$ s and last about 60s. The Data is taken for post processing between the first converged oscillation ($t \approx 30$ s) and before carriage deceleration ($t \approx 73$ s). Looking at that measurement window, we can see a typical evolution of lift (F_y) that increases as $\alpha(t)$ increases, and stall before it reaches its maximum α. The strain ϵ_1 globally matches with the lift forces, as the main deformation component is bending, which is in the lift direction. The variation of the F_z force is due to the free surface oscillation near the hull side (see Fig. 9). It generates a variation of the water depth seen by the hydrofoil's circular root interface (which is geometrically purely horizontal, hence submitted to pressure is z direction), hence changing the hydrostatic component measured by the hydrodynamic balance. It actually correlates quite well, i.e. the diminution of F_z corresponds to an increase of the lift force F_y, directly linked to an increase of negative pressure at suction side of the hydrofoil that generates free surface deflection.

Filtering and averaging procedure

Raw data were processed in order to filter noises while preserving main physical information. For static runs, the signals were averaged on the entire measurement window. For dynamic runs, a low-pass FFT filter was applied on the largest part of the signals containing complete hydrofoil oscillations. The cutoff frequency f_c was chosen to have a period of two convective times: $f_c = \frac{1}{2t_c} = \frac{V}{2c}$, in order to filter oscillation due to small vortex shedding and higher frequencies related to setup vibration and noise, and thus promote data repeatability. The resulting filtered signals were then averaged over the different oscillation periods of the run. Finally, the mean signals of different test repetitions were averaged to give the final result of the test. It should be highlighted that, depending on the reduced frequency, the final results of the tests are not computed with the same number of oscillations

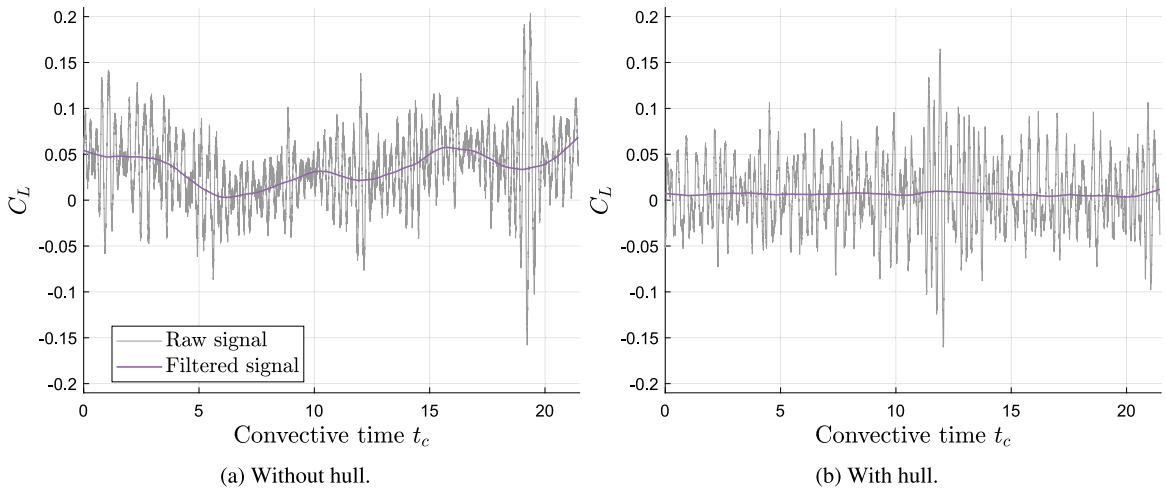

Fig. 8. Hull influence on the temporal lift coefficient evolution of the rigid hydrofoil ($Re = 500\,000$, $\alpha = 0°$).

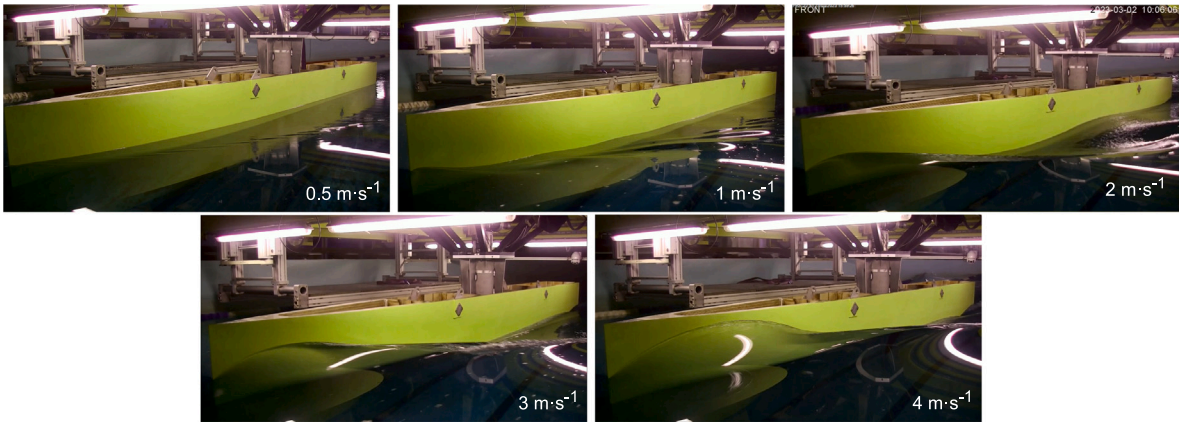

Fig. 9. Evolution of the bow wave with the carriage speed.

of the appendage. The averaged results are always computed with the maximal number of oscillations permitted by the tank length.

As an illustration, Fig. 11(a) shows results on the rigid hydrofoil from the test that gave the largest variability through test repetitions. This is due to chaotic behavior of stall condition. As a comparison, Fig. 11(b) shows a more regular result on the composite hydrofoil. The raw signals from the hydrodynamic balance are represented in light gray. The filtered signals are represented in light green and light purple, for the first and the second run respectively. The corresponding averaged signals are represented in dark green and dark purple, while the final averaged signals of the tests are plotted in black, see Fig. 11.

On Fig. 11(b) we can see an oscillating component on the raw signals that have been filtered to get the final result. This is believed to be the response of the first bending mode of the flexible hydrofoil. The frequency of the phenomenon is around 19 Hz, and can be observed regardless of the carriage speed and the hydrofoil actuation. It should be highlighted that the bending motion appears in phase with the pitching actuation resulting in oscillations of the signals superposed on each other across all pitching oscillations, even between test repetitions. Therefore, the cause of this result has not been identified yet.

For quasi-static runs, as the signals do not cover a full oscillation, the FFT filtering cannot be satisfactorily applied due to Gibbs effect. Thus, data for quasi-static runs were filtered using a linear regression over a moving time window spanning two convective times t_c.

Uncertainty analysis

The uncertainty analysis performed in this study follows the methods outlined in ASME PTC 19.1- 2005 (Dieck, 2014). In the dedicated sections the averaged results come with a total uncertainty denoted U_{tot}. This total uncertainty results from random and systematic errors. Random errors come from inherent fluctuations of a measured quantity D, and electrical noise in the system. The corresponding uncertainty is quantified as the standard deviation $s_{\bar{D}}$ of the averaged given quantity, through test repetition. Systematic uncertainties, denoted U_{sys}, depends on instrument calibration and sensitivity, as specified by the sensor vendor, see Table 1. As the quantities of interest result from combinations of sensor channels, the systematic uncertainties are combined accordingly. As an example, the systematic uncertainty on the lift coefficient, U_{C_L}, is computed as:

$$U_{C_L} = \frac{U_{F_{\tilde{x}}} |\sin(\alpha)| + U_{F_{\tilde{y}}} \cos(\alpha)}{\frac{1}{2}\rho V^2 S} \tag{1}$$

Where $U_{F_{\tilde{x}}}$ and $U_{F_{\tilde{y}}}$ are the systematic uncertainties of the forces $F_{\tilde{x}}$ and $F_{\tilde{y}}$, measured by the hydrodynamic balance. Finally, the data presented in the dedicated sections comes with the 95% confidence intervals computed as $0.95 \times U_{tot}$, where the total uncertainty is given by $U_{tot} = \sqrt{s_{\bar{D}}^2 + U_{sys}^2}$. The confidence intervals are represented by error bars for static results, and by color strips for quasi-static and dynamic results.

2.5. Validation

The reliability of the experimental setup is assessed through comparison with literature data. Static and dynamic lift coefficients from subsonic wind tunnel experiments are considered. The static data come from de Paula (2016) and Abrantes et al. (2017). The authors used

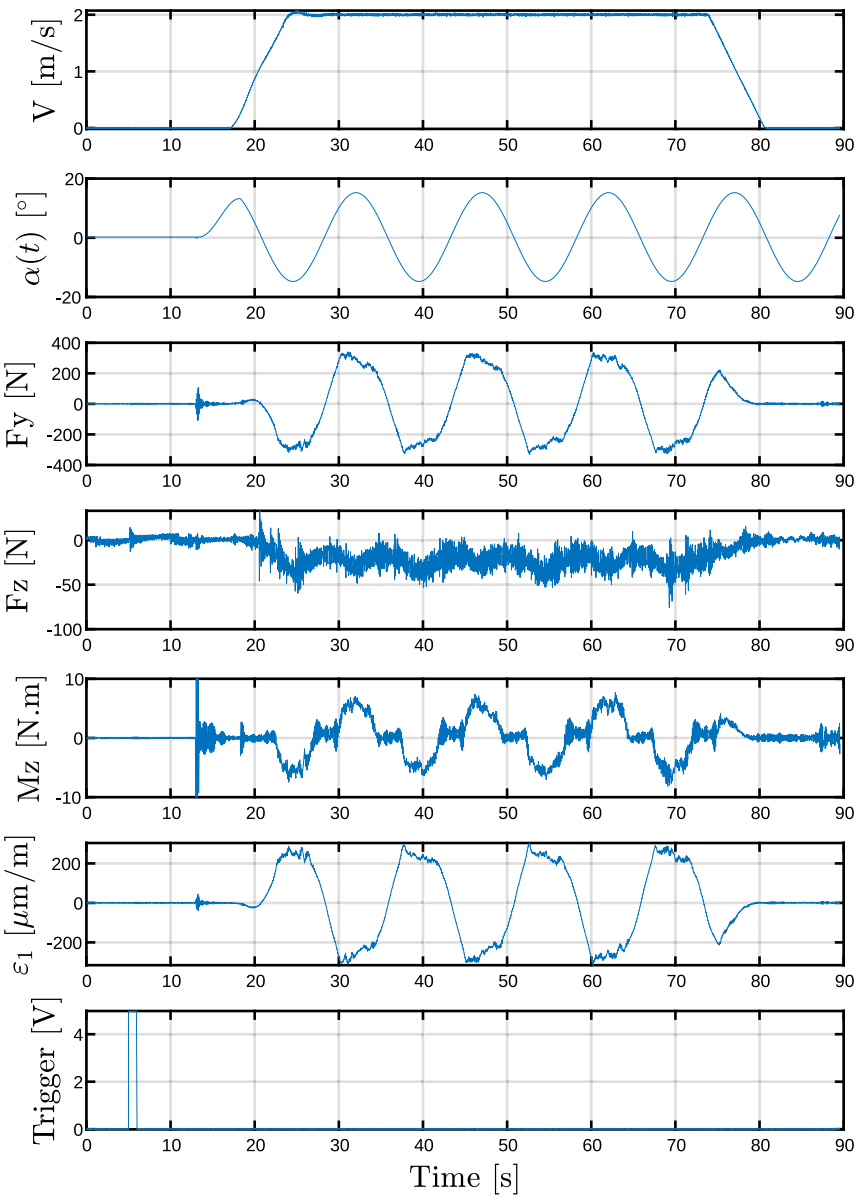

Fig. 10. Raw temporal signals for the composite hydrofoil, V =2 m·s^{-1}, k = 0.017.

respectively a pseudo-2D NACA0020 airfoil, and a similar rectangular foil with aspect ratio AR = 2, operating at Reynolds numbers Re = 200 000 and 290 000. The dynamic results are taken from Holst et al. (2019). The authors used a pseudo-2D NACA0021 airfoil pitched from its quarter-chord with a reduced frequency k = 0.05, and a Reynolds number Re = 140 000. These data are compared with present results obtained at Re = 250 000, and k = 0.05 with the rigid NACA0020 hydrofoil.

The quasi-static and static results are shown on Fig. 12(a). The dashed-line from the quasi-static result indicates the decreasing part of the angle of attack. The present values lie slightly lower than the 3D results from Abrantes et al. (2017), this may comes from the different blockage effects in both experiments. The 3D effect appears however well predicted. The black dashed line indicate the results obtained with a 3D non-linear lifting-line method alimented by polar curves from Xfoil (Drela, 1989). The slope of the linear part of the lift coefficient coincide well with the results of Abrantes et al. (2017) and the lifting-line results, compared to 2D curves that lie closer to the theoretical 2D thin airfoil law (black dash-dotted line). The quasi static and static lift coefficients are also very close from each other, which demonstrates the measurements accuracy. It has to be noted that a large quasi-static hysteresis effect is observed on the decreasing phase of the current lift coefficient, where the flow reattaches at 11°, whereas stall occurs around 20° on the increasing phase of pitch.

The dynamic results are shown on Fig. 12(b). The data from Holst et al. (2019) correspond to airfoil harmonically pitched in light dynamic stall regime (from 0° to 20°, green curve), and deep dynamic stall regime (from 10° to 30°, red curve). The present data correspond to a pitched cycle from −25° to 25°. The curve hysteresis coincides with the light dynamic stall regime. Additionally, the correspondence of the maximal lift coefficient reached at around α = 25° with the deep dynamic stall regime is satisfactory.

The results of Figs. 12(a) and 12(b) come with large uncertainties. This is due to the low speed required with the carriage to operate at Reynolds number Re = 250 000 with the rigid hydrofoil. The low hydrodynamic loadings obtained are associated with maximal uncertainties, based on the full measuring range of the hydrodynamic balance, see Table 1. However, the variability through test repetitions is very satisfactory, leading to significantly smaller uncertainties for higher carriage velocities.

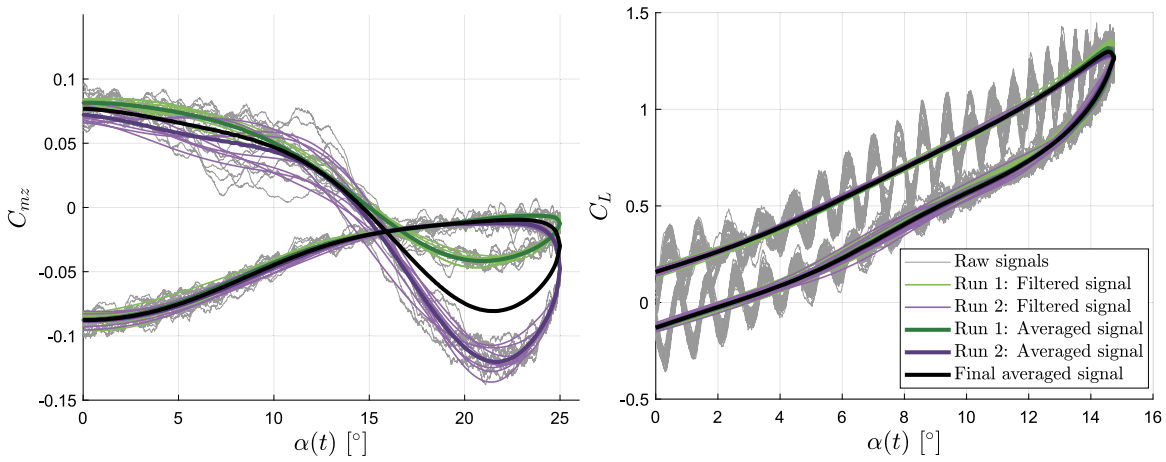

(a) Half moment coefficient of the rigid hydrofoil, $Re = 500\,000$, $k = 0.14$.

(b) Half lift coefficient of the flexible hydrofoil, $Re = 330\,000$, $k = 0.05$.

Fig. 11. Illustration of the filtering and averaging process for dynamic tests.

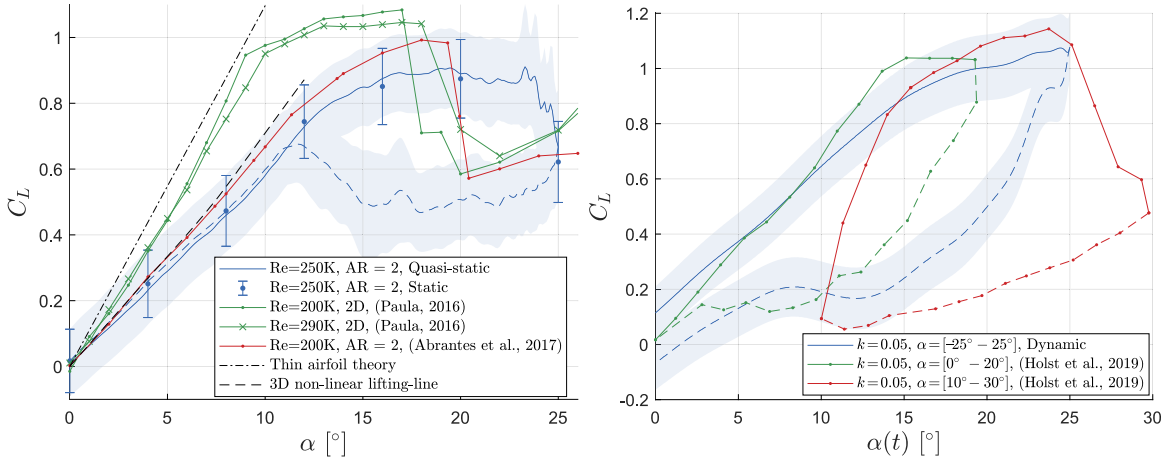

(a) Comparison of static lift coefficient from present experiments and literature data. Dashed-line indicates the decreasing phase of the angle of attack.

(b) Comparison of dynamic lift coefficient from present experiments and literature data. Dashed-line indicates the decreasing phase of the angle of attack.

Fig. 12. Validation of the experimental setup.

3. Results and discussion

The dynamic stall regime of both rigid and flexible hydrofoils is studied by means of the influence of the Reynolds number and the pitching reduced frequency on the hydrodynamic coefficients and strains (in the case of the flexible hydrofoil).

For readability purposes, the uncertainties are only shown on Fig. 13. The uncertainties for all other figures are qualitatively similar to those of Fig. 13. Tabulated data with uncertainties of all figures presented in the Results section are available as supplementary material associated with the article. Dashed lines on every figures indicate the decreasing part of the angle of attack.

3.1. Rigid hydrofoil

3.1.1. Influence of the Reynolds number

Fig. 13 shows the static and quasi-static lift and pitching moment coefficients for the different Reynolds numbers considered. The full hysteresis of the hydrodynamic coefficients is available only for the lower Reynolds number $Re = 250\,000$, because of the shorter carriage acceleration time required, allowing a longer measuring window. The static results are in good agreement with quasi-static results up to $\alpha = 12°$, and deviate moderately for higher angles of attack. All lift coefficients show a linear behavior up to $\alpha \approx 9°$, which is the consequence of mostly attached boundary layer flow along the chord. Starting from $\alpha \approx 9-10°$, the slope of the lift coefficient at $Re = 250\,000$ increases, followed by a slight decrease at about $\alpha \approx 13°$, highlighting a classical trailing edge flow detachment up to the maximum angle of attack. The development of trailing edge detachment is supported by the sudden break of C_{mz} after about $\alpha \approx 9°$, see Fig. 13(b). It is clearly identified as a displacement of center of pressure toward the trailing edge due to development of detached boundary layer. This behavior is reduced at $Re = 500\,000$ and $Re = 1\,000\,000$, due to Reynolds effects. The lift coefficient for $Re = 1\,000\,000$ show a critical angle of attack at $\alpha = 17°$. But there is no clear critical angle of attack visible for the two lower Reynolds numbers. Instead, the lift slopes progressively decrease and become negative around $\alpha \approx 19°$.

Uncertainties strips remain mostly similar for stalled regime and attached regime, highlight the satisfactory repeatability of the quasi-static results. The average pitching rate of the quasi-static tests at $Re = 250\,000$ is $0.25° \text{ s}^{-1}$. The corresponding reduced pitch rate proposed by Le Fouest et al. (2021) is $\frac{\dot{\alpha}c}{2V} = 2.2\times10^{-3}$, which is above the limiting

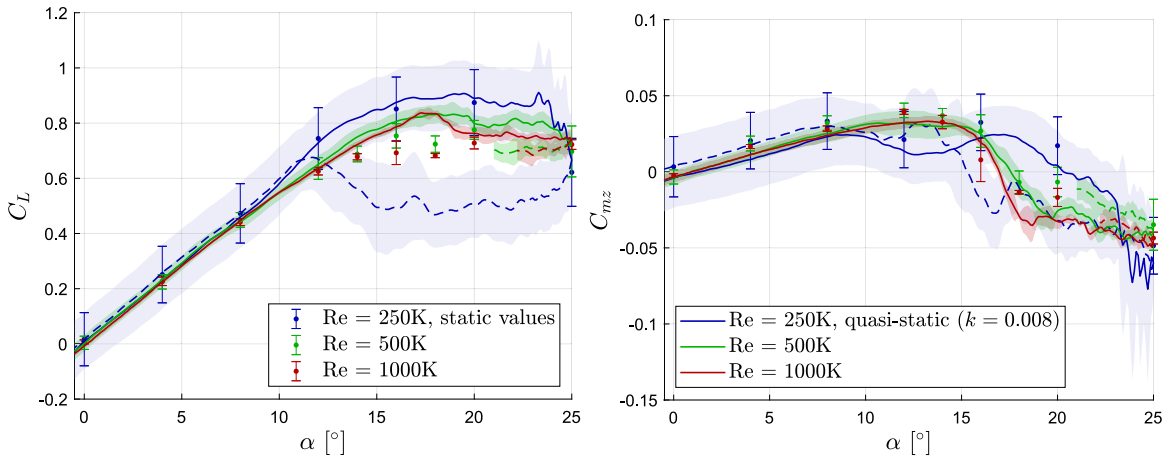

(a) Lift coefficient. (b) Moment coefficient.

Fig. 13. Influence of the Reynolds number on static and quasi-static hydrodynamic coefficients of the rigid hydrofoil. Color stripes and error bars indicate uncertainties. Dashed lines indicate the decreasing part of the angle of attack.

value 10^{-4} in order to be classified as quasi-static motion. However, the decreasing phase of the angle of attack from $\alpha = 25°$ to $10°$ lasts about 70 s, which is almost two order of magnitude higher than the convective time of the flow: $t_c = \frac{c}{V} = 1$ s. Therefore, by also considering the good repeatability of the measurements, the hysteresis shown on Fig. 13 is more likely to reflect a quasi-static nature rather than being a result of dynamic effects.

Fig. 14 shows the influence of the Reynolds number on the hydrodynamic coefficients, for three reduced frequencies. The corresponding figures for the remaining reduced frequencies can be found in the appendix. At reduced frequency $k = 0.025$, the behavior of the hydrodynamic coefficients is qualitatively similar than for the quasi-static results. The lift reach however higher values of about $C_L = 1$ as compared to $C_L = 0.9$ for the quasi-static case. The influence of Reynolds number is significant from $Re = 250\,000$ to $Re = 500\,000$, whereas it is reduced between $Re = 500\,000$ and $Re = 1\,000\,000$. After 10°, the non-linearity on the lift coefficient associated with the development or trailing edge vortex at $Re = 250\,000$ disappears for the higher Reynolds numbers, as well as the hysteresis, which is significantly reduced. The critical angle of attack appears to be the same for the three Reynolds numbers at about 20°. The moment coefficient in Fig. 14(b) shows an expected behavior: it is small and slightly increases from 0° to 20° due to the shift of the center of pressure toward the leading edge, and decreases abruptly when stall occurs. During the decreasing phase, it get back to the initial slope at the early stage of the reattachment at 13°. The hydrodynamic coefficients curves becomes smoother for the higher reduced frequency, i.e. $k = 0.14$, indicating the decrease of stochastic variations induced by viscous effects. No critical angle of attack is observed for the higher reduced frequency. The larger variation is observed on the moment coefficient in Fig. 14(f) in the decreasing phase, where the dynamic stall may delay the convection of leading edge vortex through the hydrofoil's chord, inducing a strong variation of the center of pressure. The case as $k = 0.05$ in a transition case between dynamic and quasi-static. Hysteresis effects are observed for the lower Reynolds number ($Re = 250000$ in Fig. 14(c)) and tends to completely disappear for the higher Reynolds numbers. The hydrodynamic coefficients also clearly start to show the influence of forced pitching motion highlighted by global increase of lift and moment coefficient in the attached regions of angle of attacks.

The present analysis of Reynolds number effects may also supports the conjecture of Choudhry et al. (2014), that says that the dynamic stall process is greatly influenced by the state of the boundary layer prior to any unsteadiness. As there is no or low incoming turbulence intensity, there could be some highly transitional regimes at $Re = 250\,000$. For higher reduced frequencies, the profile acceleration becomes dominant on hydrodynamics coefficients. Thus, Reynolds effect is less visible in the increasing phase of the angle of attack. Vortex shedding are more likely to occurs on the decreasing phase of the angle of attack.

Despite modest stochastic variations from cycle to cycle and from test repetition, data tend to cluster to a single averaged behavior, which contrasts with the observations of Holst et al. (2019). The reason may come from the finite number of oscillations permitted by the tank length, or also by the significant 3D effects promoting a particular group of fluctuations.

3.1.2. *Influence of the reduced frequency*

Fig. 15 shows the effect of the reduced frequency k on the hydrodynamics coefficients, for the three Reynolds numbers considered. Part of the data presented are identical to those of Fig. 14, but the curves are arranged to highlight the pitching frequency effect on the dynamic stall behavior. The complete reduced frequency measurement are shown in this figure. Dark color lines represent low reduced frequencies and light color lines represent high reduced frequencies.

For all Reynolds numbers, the maximal lift coefficient increases with the reduced frequency up to $k = 0.08$, which is consistent with the literature, and is attributed to the delay of stall onset, (Choudhry et al., 2014; Jumper et al., 1987; Gardner et al., 2023). In addition, the flow reattachment process tends to disappear with increasing k, leading to a practically convex C_L curves for $k = 0.14$. This characteristic has been extensively designated as light dynamic stall, (McCroskey et al., 1981; Choudhry et al., 2014). The more precise definition of light and deep dynamic stall proposed by Mulleners and Raffel (2012) is based on the stall onset. In the present work, stall onset cannot be precisely identified but it appears with the appearance of the hydrodynamic loading that the transition between deep dynamic stall and light dynamic stall occurs between $k = 0.05$ and $k = 0.14$, for Reynolds number $Re = 250\,000$, see Fig. 15(a).

As k increases, the profile acceleration becomes dominant on the hydrodynamic coefficients. Hence, the viscous effects are reduced, and consequently the hysteresis progressively disappears, and the lift and moment coefficients at $\alpha = 0°$ increase. The reduction of the viscous effects is also highlighted by the sharp decrease of C_{mz} after $\alpha \approx 18°$ for $k = 0.025$, which disappear at $k = 0.14$. The maximal values of C_{mz} are reached at $\alpha = 0°$, where the pitching velocity is maximal. In contrast, for lower k, maximal values of C_{mz} are reached at the maximal angle of attack $\alpha = \pm\alpha_{max}$.

For Reynolds numbers $Re = 500\,000$ and $1\,000\,000$, the maximal lift coefficients are reach around $\alpha = 21.5°$ and $\alpha = 24°$ for $k = 0.025$ and

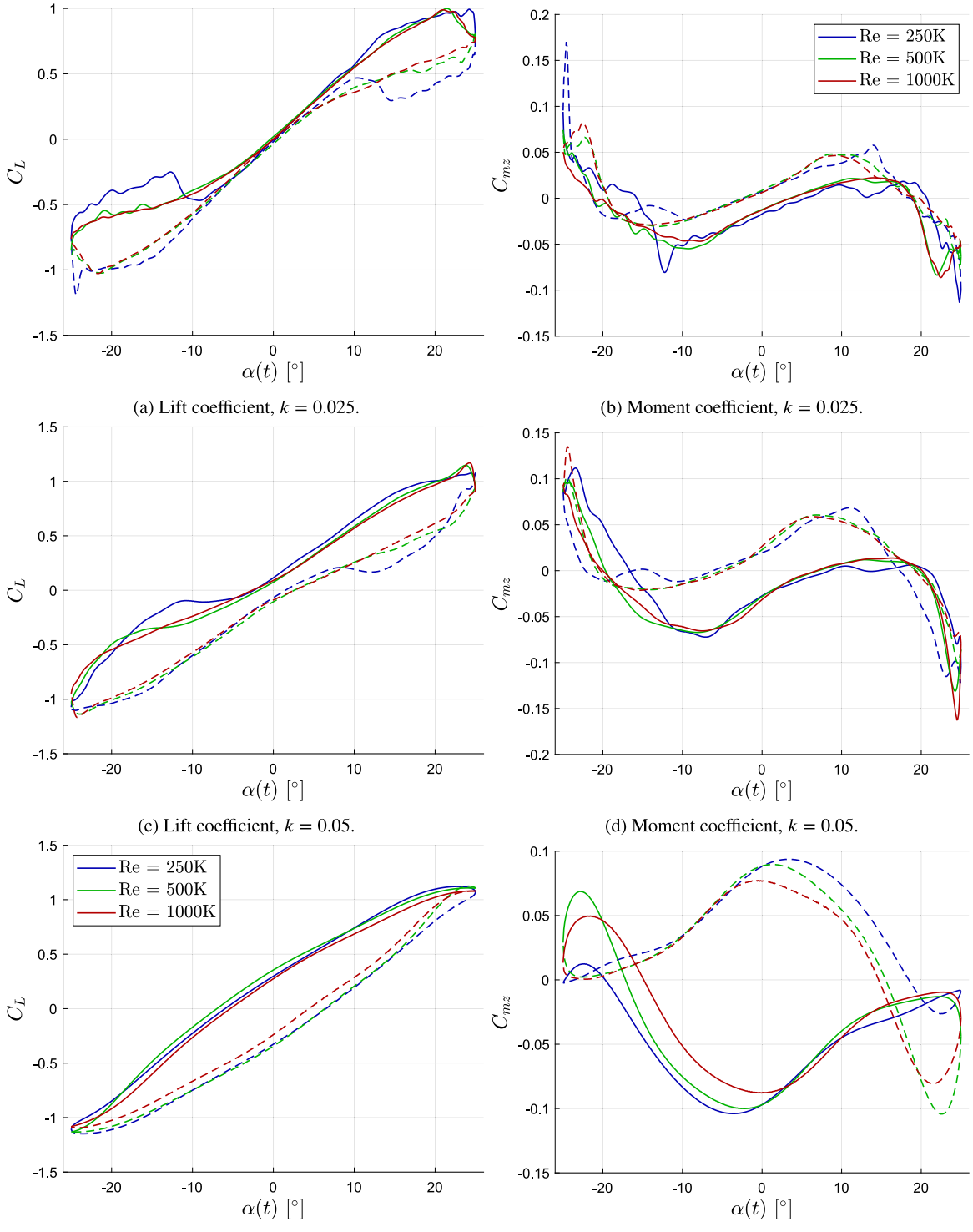

(a) Lift coefficient, $k = 0.025$.

(b) Moment coefficient, $k = 0.025$.

(c) Lift coefficient, $k = 0.05$.

(d) Moment coefficient, $k = 0.05$.

(e) Lift coefficient, $k = 0.14$.

(f) Moment coefficient, $k = 0.14$.

Fig. 14. Influence of the Reynolds number on dynamic hydrodynamic coefficients of the rigid hydrofoil. Dashed lines indicate the decreasing part of the angle of attack.

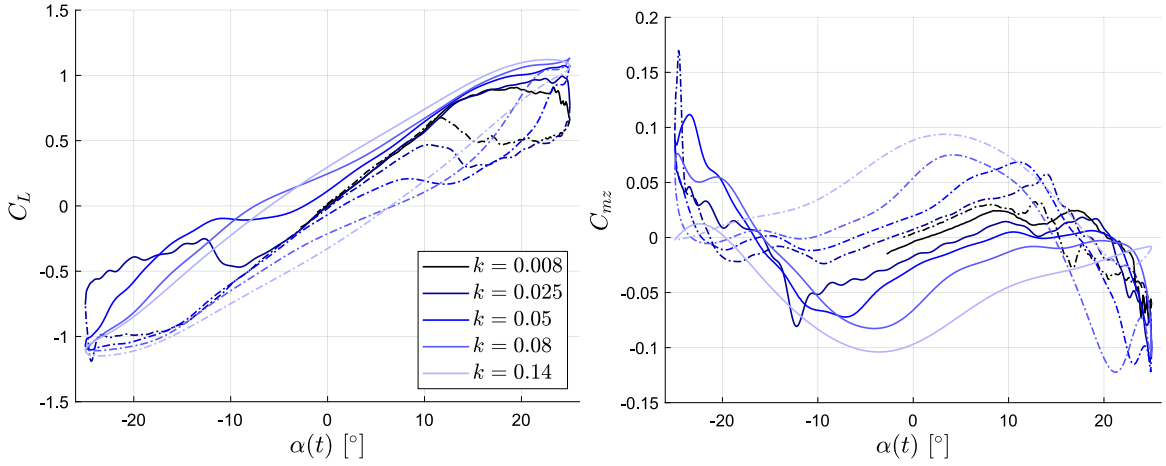

(a) Lift coefficient, $Re = 250\,000$.

(b) Moment coefficient, $Re = 250\,000$.

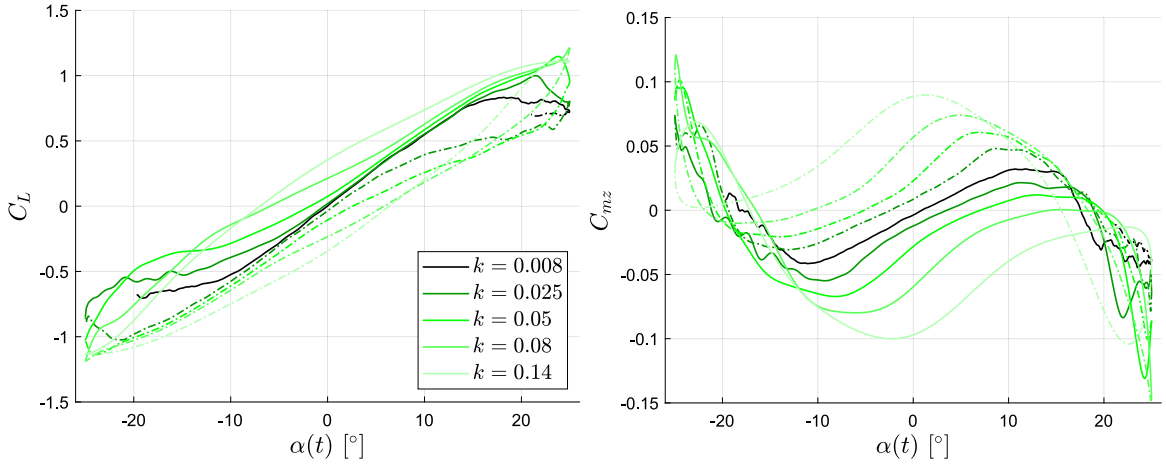

(c) Lift coefficient, $Re = 500\,000$.

(d) Moment coefficient, $Re = 500\,000$.

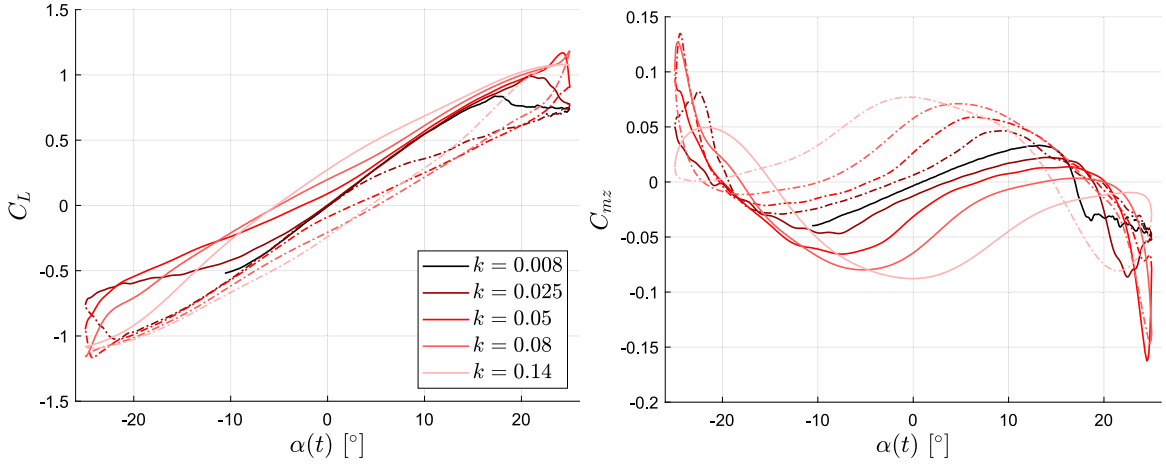

(e) Lift coefficient, $Re = 1\,000\,000$.

(f) Moment coefficient, $Re = 1\,000\,000$.

Fig. 15. Influence of the reduced frequency on dynamic hydrodynamic coefficients of the rigid hydrofoil. Dashed lines indicate the decreasing part of the angle of attack.

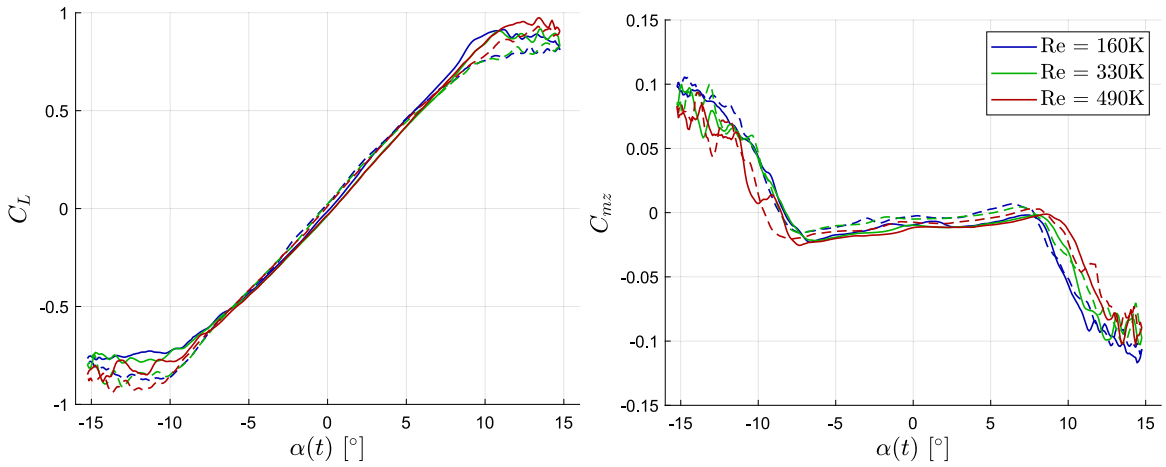

(a) Lift coefficient, $k = 0.0085$.

(b) Moment coefficient, $k = 0.0085$.

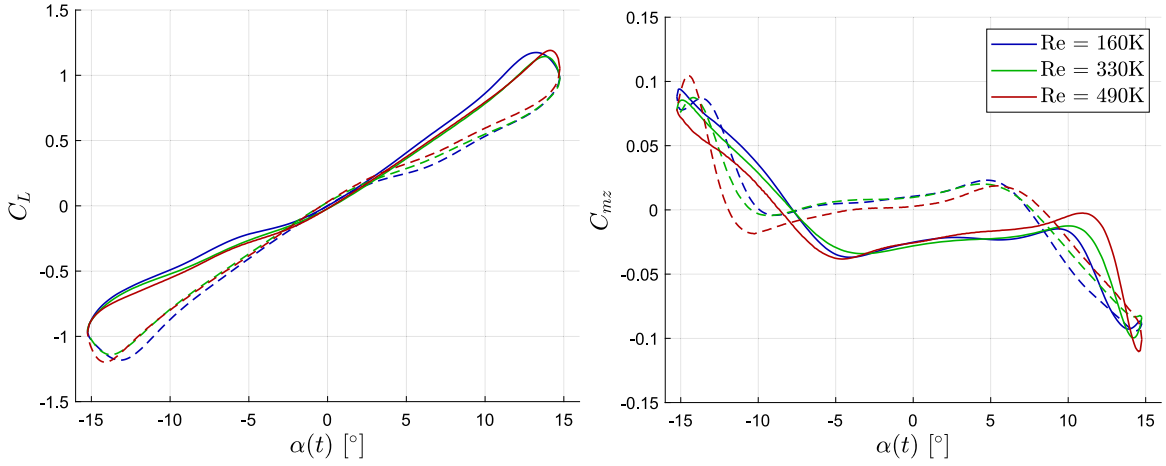

(c) Lift coefficient, $k = 0.05$.

(d) Moment coefficient, $k = 0.05$.

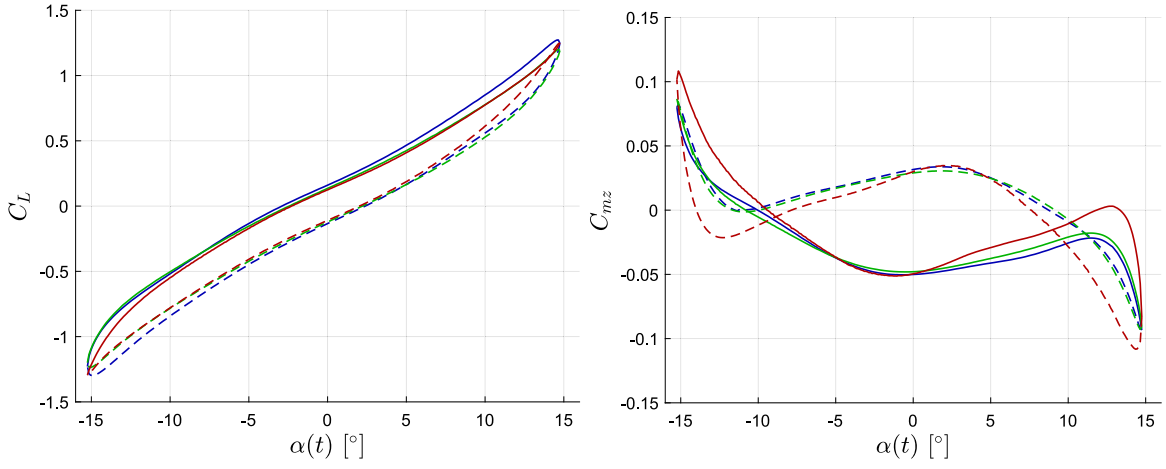

(e) Lift coefficient, $k = 0.1$.

(f) Moment coefficient, $k = 0.1$.

Fig. 16. Influence of the Reynolds number on dynamic hydrodynamic coefficients of the flexible hydrofoil. Dashed lines indicate the decreasing part of the angle of attack.

0.05 respectively. Whereas the maximal lift coefficient is reached at the maximal angle of attack for higher reduced frequencies. The sudden decrease of the lift is associated with the detachment of the dynamic stall vortex. It appears on Fig. 15 that for reduced frequencies $k = 0.08$ and 0.14, the dynamic pitch motion leads to a decreasing angle of attack before the detachment of the dynamic stall vortex. Moreover, at $k = 0.08$, the lift coefficient curve around $\alpha \approx 23°$ is convex, indicating the motion of the dynamic stall vortex along the profile suction side. This is supported by the drop of the moment coefficient revealing the displacement of the pressure center. Then, the profile angle of attack starts to decrease before the dynamic stall vortex reach the trailing edge region and detaches. In contrast, at $k = 0.14$ the lift coefficient curve around $\alpha \approx 23°$ is concave, indicating that the motion of the profile leads to an decreasing angle of attack during the formation of the dynamic stall vortex, and thus before the beginning of its motion, as portrayed by the lower drop of the moment coefficient around the maximal angle of attack for $k = 0.14$.

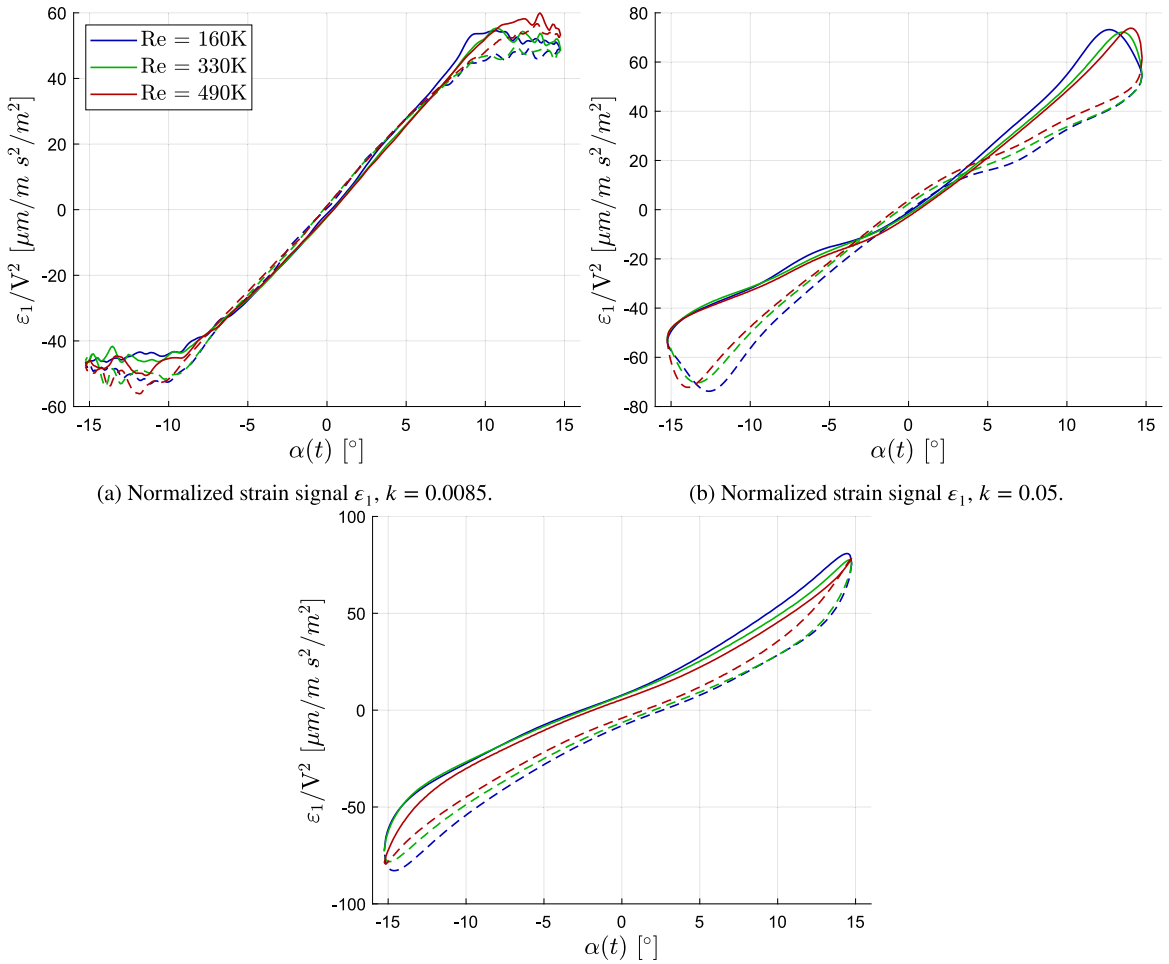

(a) Normalized strain signal ε_1, $k = 0.0085$.

(b) Normalized strain signal ε_1, $k = 0.05$.

(c) Normalized strain signal ε_1, $k = 0.1$.

Fig. 17. Influence of the Reynolds number on strain signal of the flexible hydrofoil. Dashed lines indicate the decreasing part of the angle of attack.

3.2. Flexible hydrofoil

The dynamic stall behavior of the flexible hydrofoil is studied by mean of influence of the Reynolds number and the reduced frequency on the hydrodynamic coefficients and on the strain signal from ε_1 sensor, see Fig. 4. In order to compare strains from various Reynolds numbers, the signals are normalized by the carriage speed squared. Moreover, in order to get insight on the influence of the spanwise location on strain, strain data from various FBG sensors are shown for particular values of Re and k.

3.2.1. Influence of the Reynolds number

Fig. 16 shows the lift and moment coefficients of the flexible composite hydrofoil for Reynolds numbers ranging from $Re = 160\,000$ to $490\,000$, for three reduced frequencies. The corresponding figures for the remaining reduced frequencies can be found in the appendix. As it is a thin profile (NACA0006) the behavior of the flexible hydrofoil is close to what is expected with a flat plate. For the lower reduced frequency ($k = 0.0085$), the lift shows a linear behavior up to around 9° and then stall quickly, see Fig. 16(a). The pitching moment stay constant close to zero before stall, as the center of pressure does not move with the angle of attack, and is close to the center of rotation. Then the moment coefficient drops, clearly highlighting the boundary layer detachment. Stall is slightly delayed as Re increases, whereas the hysteresis effect decreases. At higher reduced frequency of $k = 0.1$ (Figs. 16(e) and 16(f)), the viscous effects have completely disappear and the hydrodynamic coefficients are submitted to the pressure field induced by the forced pitching motion. The lift coefficient curves are very similar for the different Reynolds numbers and show convex and concave shapes characteristics of dynamic motion. Discrepancies are found for the moment coefficient. As the chord is rather small, this may be due to a slight displacement of the center of pressure due to dynamic stall. The case at $k = 0.05$ (Figs. 16(c) and 16(d)), is clearly a transitioning case as for the rigid hydrofoil. Lift coefficient remains linear as the profile pitch positively. Stall is then slightly delayed as Reynolds number increases, and as the angle of attack decreases, the coefficients are submitted to both the effect of vortex shedding and pitching motion effects. The effect of Reynolds number is significantly lower as compared to the rigid, thick hydrofoil, which is expected.

Fig. 17 show the strains ε_1 as function of the Reynolds number for the three reduced frequencies analyzed previously for the hydrodynamic coefficients. The signals are very similar to the lift coefficient curves, highlighting the structural response of the hydrofoil in bending due to hydrodynamic loading. The stall angle of attack remains the same as for the lift coefficient, which means that the structure responds almost instantaneously to the hydrodynamic loads. The dynamic pitching motion seems however more pronounced than for the lift coefficient, which may come from structural inertia effect.

To demonstrate the strain measurement accuracy through FBG sensors, the strains distribution during pitch is analyzed in Fig. 18, for the lower and higher Reynolds numbers and reduced frequencies tested. Strains from ε_1 (near the root) to ε_5 (near the tip) are selected, see Fig. 4. As expected, the strain is maximum near the root ε_1 and decreases progressively as we move close to the tip of the hydrofoil,

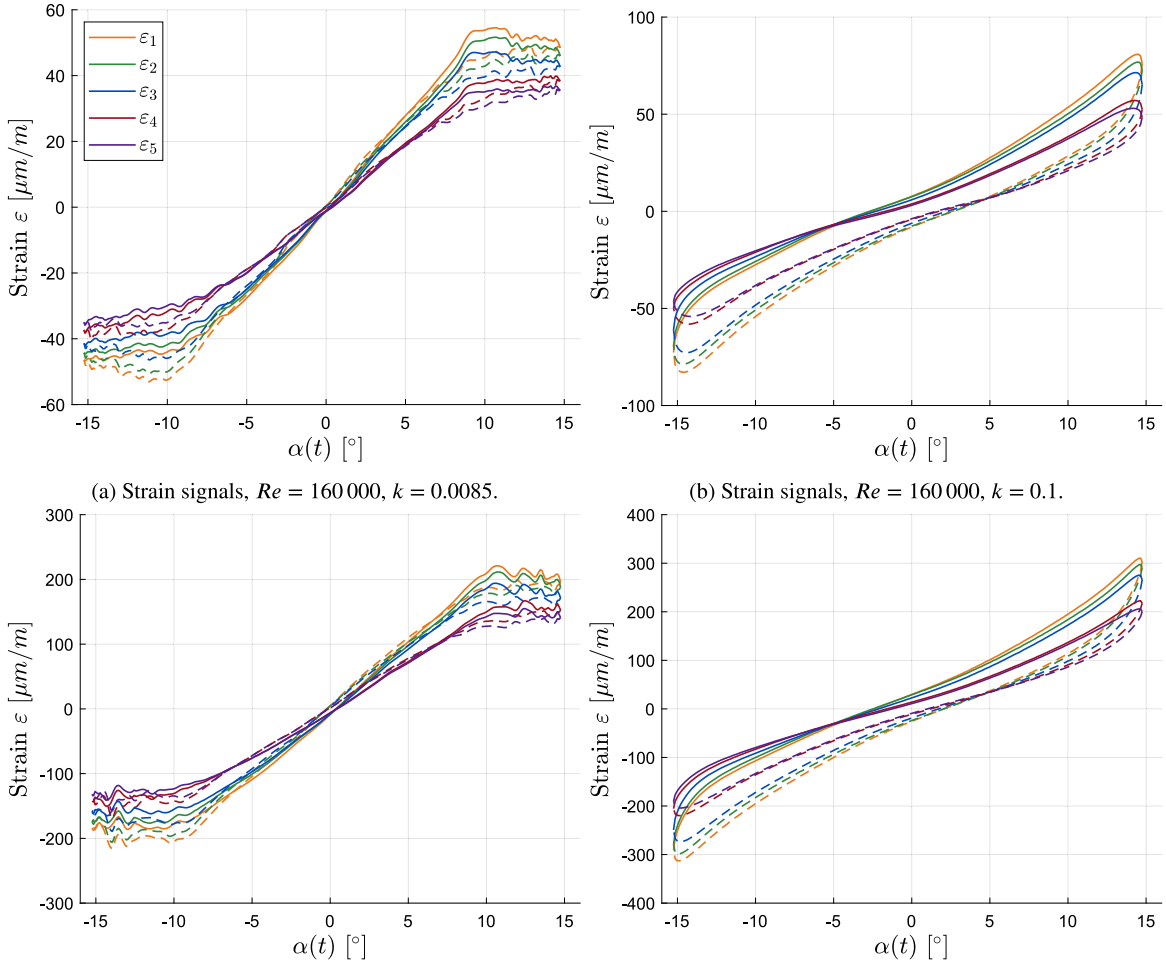

(a) Strain signals, $Re = 160\,000$, $k = 0.0085$.

(b) Strain signals, $Re = 160\,000$, $k = 0.1$.

(c) Strain signals, $Re = 490\,000$, $k = 0.0085$.

(d) Strain signals, $Re = 490\,000$, $k = 0.1$.

Fig. 18. Strain signals from various sensors along the span of the flexible hydrofoil. Dashed lines indicate the decreasing part of the angle of attack.

where the deflection is maximum. The minimum strain is obtained at 0° of angle of attack for all the sensors and all the cases, and signals are purely symmetrical for positive and negative angles of attacks. For the lower reduced frequencies, the tip strain ε_5 (see dark purple lines in Figs. 18(a) and 18(c)) continues to slightly increases after stall onset, which can be explained by a modification of the pressure distribution due to the development of 3D flow detachment along the hydrofoil's span.

3.2.2. *Influence of the reduced frequency*

The influence of pitching frequency on the hydrodynamic coefficients is represented in Fig. 19, for the three Reynolds numbers considered. As for the rigid hydrofoil, the dark color lines represent the low reduced pitching frequencies whereas the light color lines represent the high reduced frequencies. When available, the static hydrodynamic coefficients are also displayed for comparison. For the lift coefficient, the lower pitching frequency lies very well with the static values before stall onset. The low number of static measurements after stall is not sufficient to perform the analysis for high angles of attacks. The comparison with static measurement shows a clear difference on the moment coefficient, where it is lower in the attached flow range of angle of attacks (0° to 10°), see the comparison of black lines with dark colored lines in Figs. 19(b) and 19(f). The difference increases with the Reynolds number. This effect has not been observed on the rigid hydrofoil, see Fig. 13. The dynamic moment coefficients of the flexible hydrofoil are characterized by a clear asymmetry, visible at 0° where $|C_{mz}|$ should be identical. The reason given for this discrepancy is an hysteresis on strains. This statement have to be confirmed through coupled fluid–structure calculations in the near future.

The increase of reduced frequency delays the stall onset, up to the higher reduced frequency ($k = 0.1$), where stall is removed. As the increase of Reynolds number tends to delay the critical angle of attack and reduces the hysteresis effect, the effect of pitch frequency is larger for lower Reynolds numbers. The pitching dynamics also bring a difference between decreasing and increasing angles of attacks, as observed for the rigid hydrofoil, due to the wall pressure component added by the profile acceleration. It has to be noted that the curve shapes with high dynamic differs between both hydrofoils, where the concave and convex shapes are reversed. This is due to the different rotation axis relative to center of pressure i.e. acting point of the lift. The rigid hydrofoil is rectangular and pitch about its quarter of the chord whereas the composite hydrofoil pitch about its mid chord at the root, with an inclined leading edge.

4. Conclusions

This paper present results from a new experimental setup in the towing tank at Centrale Nantes. The setup was developed to measure the hydrodynamics of moderate to large scale innovative appendages (span×chord $\approx$ 1× 0.5 m, $Re \approx 1\,000\,000$). The original feature of the

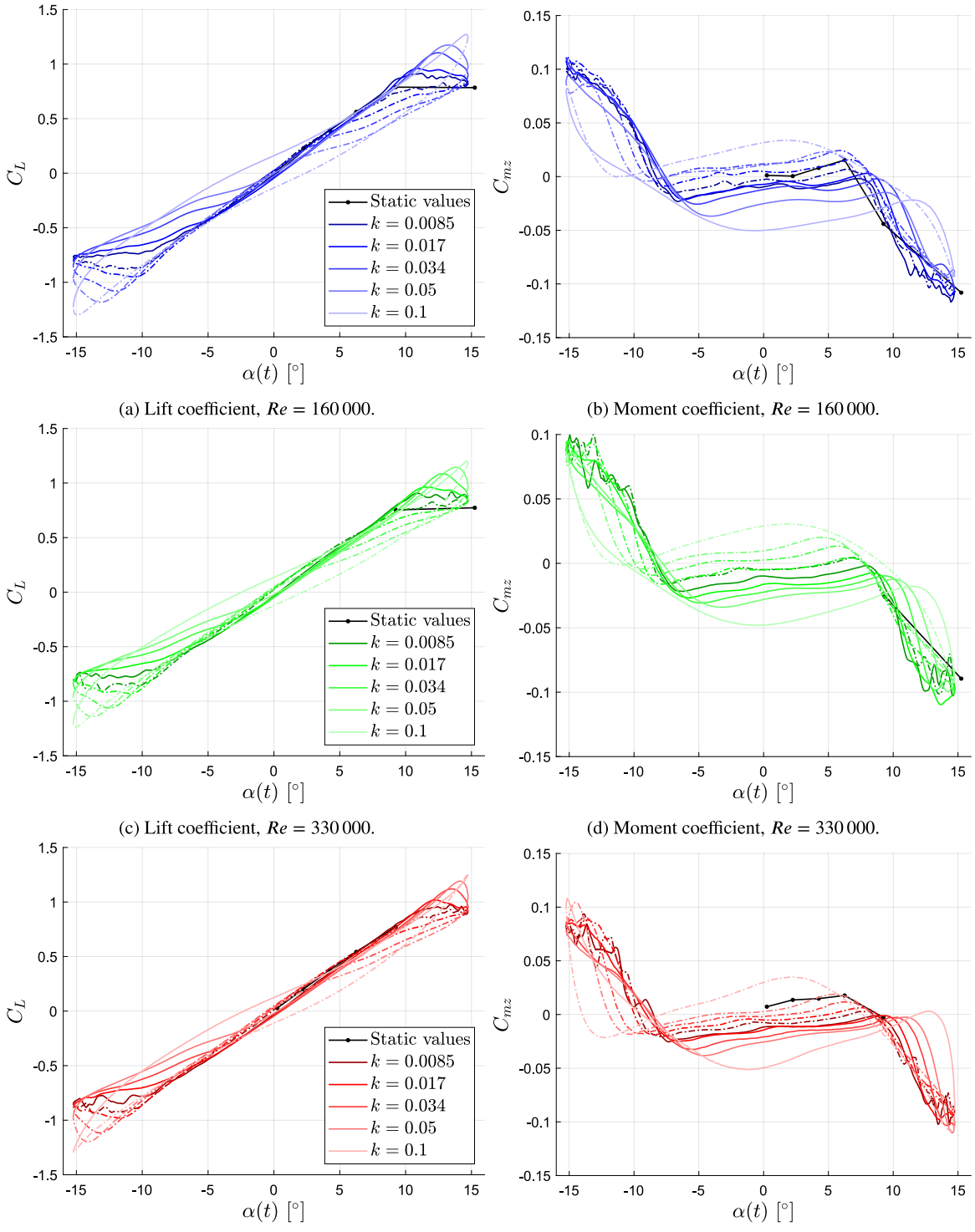

(a) Lift coefficient, $Re = 160\,000$.

(b) Moment coefficient, $Re = 160\,000$.

(c) Lift coefficient, $Re = 330\,000$.

(d) Moment coefficient, $Re = 330\,000$.

(e) Lift coefficient, $Re = 4900\,000$.

(f) Moment coefficient, $Re = 490\,000$.

Fig. 19. Influence of the reduced frequency on dynamic hydrodynamic coefficients of the flexible hydrofoil. Dashed lines indicate the decreasing part of the angle of attack.

setup is its capability to simultaneously induce dynamical pitching motions to the appendages, and measure strains and hydrodynamic performances. After a series of tests to characterize the system, the experimental setup accuracy was demonstrated through a detailed study of the influence of the Reynolds number and the reduced frequency, on hydrodynamic coefficients and strains of two pitching appendages, with dynamic stall regimes. The first appendage is a rigid rudder-like hydrofoil, while the second one has the geometry of a simplified propeller blade. The latter is made of prepreg carbon fiber reinforced epoxy, and it is equipped with optical fibers with arrays of fiber bragg gratings.

First, static and quasi-static tests were performed. The rudder-like hydrofoil performances show quite high non-linear behavior as function of the angle of attack due to large boundary layer detachments induced by both the relatively large thickness and angles of attack tested. A quasi-static hysteresis effect was also observed on the lift. The composite, thin hydrofoil shows a more linear behavior, with an earlier and sharper stall. For both hydrofoils, the effects of the Reynolds number and the reduced frequency on the hydrodynamic coefficients show some similarities. As the profile acceleration increases, the viscous effects are reduced. Thus, the stall onset is delayed to higher angle of attack and the hysteresis tends to disappear. It has also been observed that the lift and pitching moment increases around 0°. The reduced frequency effect diminishes as the Reynolds number increases, and vice-versa. For the composite hydrofoil, a close proximity is obtained between the lift and the strain signal near the root, highlighting a structural response of the hydrofoil in bending due to hydrodynamic loading. As expected, the strain decreases progressively as we move close to the tip of the hydrofoil, where the deflection is maximum.

As the lift coefficient and the strains are assessed with independent measurement systems, their close proximity demonstrates the good accuracy of the experimental setup, and the link between lift and structural bending deformation. The data also demonstrated setup capabilities to capture subtle flow phenomena such as displacement of center of pressure, or delay of stall onset. This original setup appears thus reliable to study hydrodynamic of large lifting appendages in dynamic stall regimes. The emergence of such setup has a key role to stimulate the ongoing development of innovative appendages, and to generate experimental data to validate numerical methods.

Following this work, fluid structure interaction phenomena on the flexible hydrofoil will be addressed. In particular, spectral analysis will aim to highlight possible interactions between Strouhal and modal frequencies. In the near future, more sophisticated appendages will also be tested, and the setup will be equipped with instrumentation for flow measurement.

CRediT authorship contribution statement

Théo Simonet: Writing – original draft, Visualization, Validation, Software, Investigation, Formal analysis, Data curation. **Antoine Ducoin:** Writing – original draft, Supervision, Resources, Project administration, Methodology, Investigation, Funding acquisition, Formal analysis, Conceptualization. **Quentin Rakotomalala:** Writing – original draft, Investigation. **Mathias Riou:** Writing – original draft, Investigation. **Camille Yvin:** Writing – original draft, Investigation.

Declaration of competing interest

The authors declare that they have no known competing financial interests or personal relationships that could have appeared to influence the work reported in this paper.

Acknowledgments

This work was founded by the Carnot MERS institute (APHINOV project), and the Joint Laboratory in Maritime Technology (JLMT), which is a collaboration agreement between Centrale Nantes and Naval Group. The authors would like to thanks all the technicians and engineers from these institutions who contributed to the design and mounting of the experimental setup and the help during measurements.

Appendix A

See Figs. 20–22.

Appendix B. Supplementary data

Supplementary material related to this article can be found online at https://doi.org/10.1016/j.oceaneng.2024.119621.

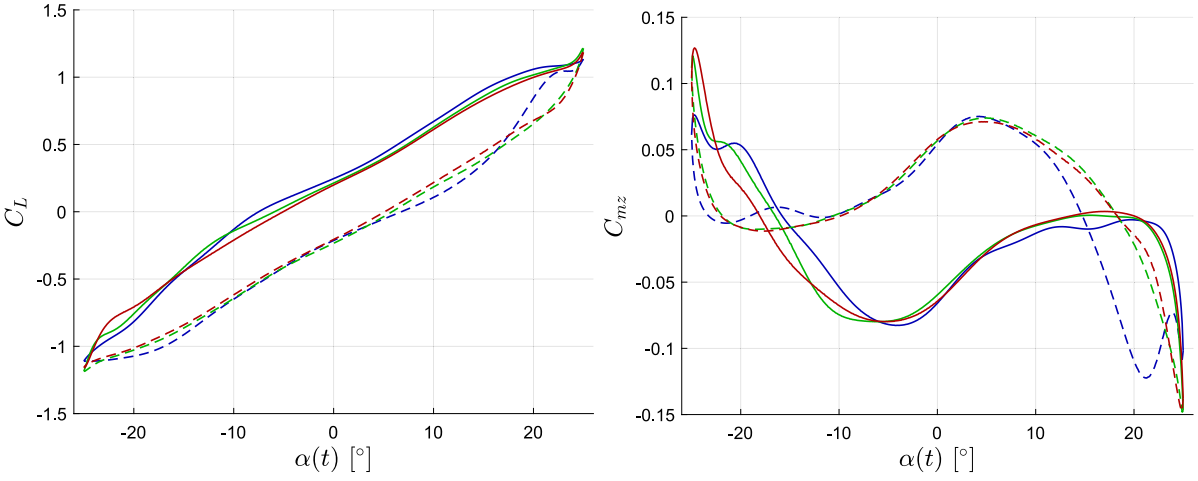

(a) Lift coefficient.

(b) Moment coefficient.

Fig. 20. Influence of the Reynolds number on dynamic hydrodynamic coefficients of the rigid hydrofoil, $k = 0.08$.

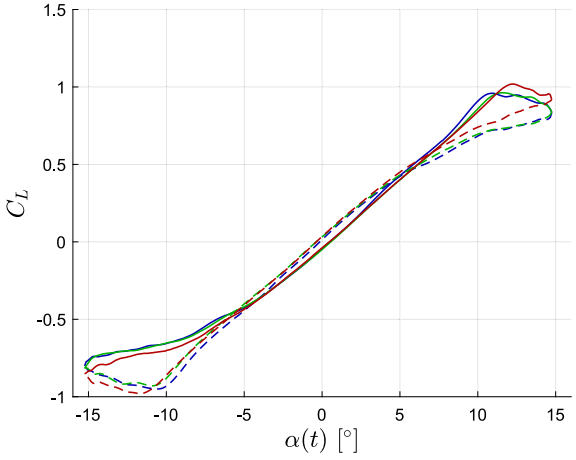

(a) Lift coefficient, $k = 0.017$.

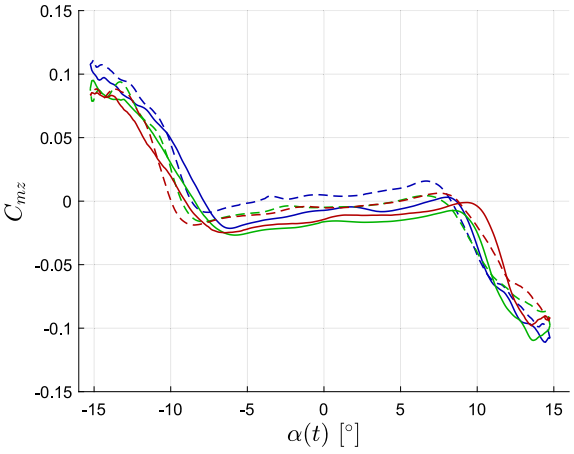

(b) Moment coefficient, $k = 0.017$.

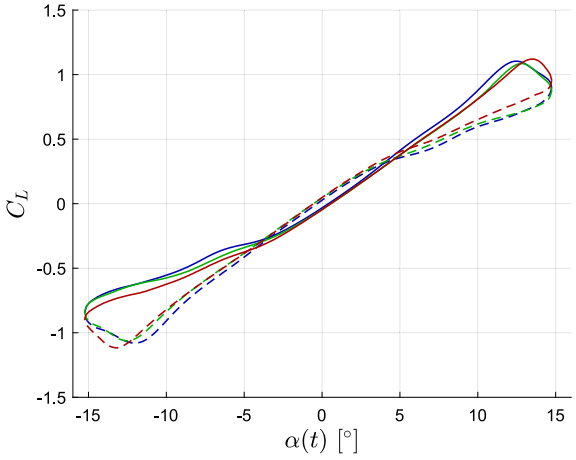

(c) Lift coefficient, $k = 0.034$.

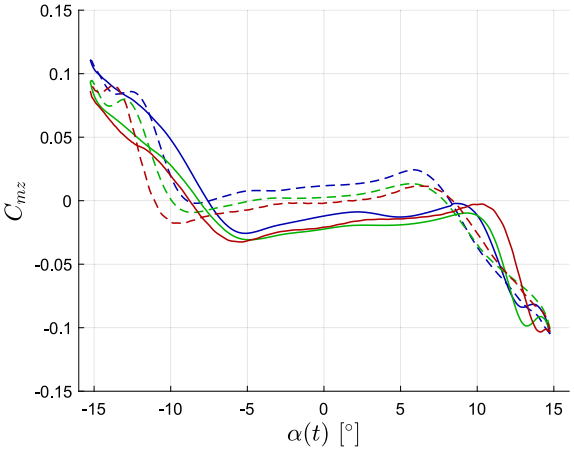

(d) Moment coefficient, $k = 0.034$.

Fig. 21. Influence of the Reynolds number on dynamic hydrodynamic coefficients of the flexible hydrofoil.

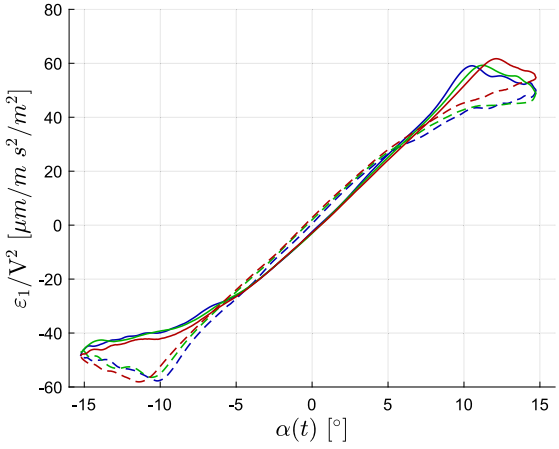

(a) Normalized strain signal ε_1, $k = 0.017$.

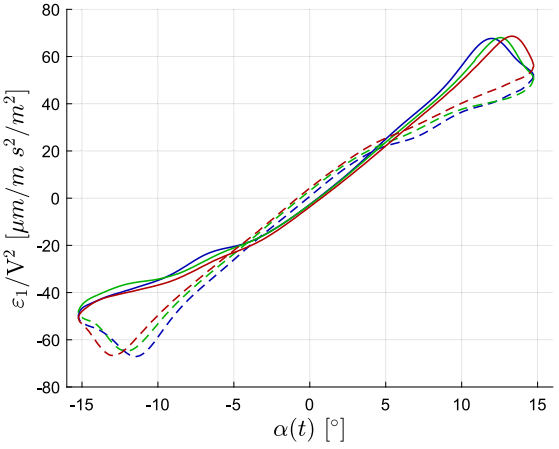

(b) Normalized strain signal ε_1, $k = 0.034$.

Fig. 22. Influence of the Reynolds number on strain signal of the flexible hydrofoil.

Data availability

Tabulated data with uncertainties of all figures presented in the Results section are available as supplementary material associated with the article.

References

Abrantes, T.T.D., Rios Cruz, A.A., de Paula, A.A., Kleine, V.G., Büttner, F., 2017. The wing three-dimensional effects on wavy leading edge performance. In: 35th AIAA applied aerodynamics conference. p. 4467.

Akcabay, D.T., Chae, E.J., Young, Y.L., Ducoin, A., Astolfi, J.A., 2014. Cavity induced vibration of flexible hydrofoils. J. Fluids Struct. 49, 463–484.

Amini, Y., Kianmehr, B., Emdad, H., 2019. Dynamic stall simulation of a pitching hydrofoil near free surface by using the volume of fluid method. Ocean Eng. 192, 106553.

Andreu Angulo, I., Ansell, P.J., 2019. Influence of aspect ratio on dynamic stall of a finite wing. AIAA J. 57 (7), 2722–2733.

Benton, S., Visbal, M., 2019. The onset of dynamic stall at a high, transitional Reynolds number. J. Fluid Mech. 861, 860–885.

Bi, S., Cai, Y., 2012. Effect of spanwise flexibility on propulsion performance of a flapping hydrofoil at low Reynolds number. Chin. J. Mech. Eng. 25 (1), 12–19.

Bø ckmann, E., Steen, S., 2014. Experiments with actively pitch-controlled and spring-loaded oscillating foils. Appl. Ocean Res. 48, 227–235.

Bøckmann, E., 2015. Wave Propulsion of Ships (Ph.D. thesis). NTNU.

Cho, H., Lee, N., Shin, S.-J., Lee, S., 2019. Extensive 3D analysis for fluid–structure interaction of spanwise flexible plunging wing 3D FSI analysis for spanwise flexible plunging wing. Aeronaut. J. 123 (1262), 484–506.

Choudhry, A., Leknys, R., Arjomandi, M., Kelso, R., 2014. An insight into the dynamic stall lift characteristics. Exp. Therm Fluid Sci. 58, 188–208.

Choudhuri, P.G., Knight, D., 1996. Effects of compressibility, pitch rate, and Reynolds number on unsteady incipient leading-edge boundary layer separation over a pitching airfoil. J. Fluid Mech. 308, 195–217.

Cleaver, D., Calderon, D., Wang, Z., Gursul, I., 2016. Lift enhancement through flexibility of plunging wings at low Reynolds numbers. J. Fluids Struct. 64, 27–45.

Cook, P., Alavija, A., Wildy, S., 2017. Identification and characterisation of delamination damage in composites utilising embedded optical strain gauges. In: 9th Australasian Congress on Applied Mechanics. Engineers Australia, pp. 140–147.

Dieck, R.H., 2014. The purpose for measurements and understanding their uncertainties (the basic, ISO and ASME uncertainty models compared). IET.

Drela, M., 1989. XFOIL: An analysis and design system for low Reynolds number airfoils. In: Low Reynolds Number Aerodynamics: Proceedings of the Conference Notre Dame, Indiana, USA, 5–7 June 1989. Springer, pp. 1–12.

Ducoin, A., Astolfi, J.A., Sigrist, J.-F., 2012. An experimental analysis of fluid structure interaction on a flexible hydrofoil in various flow regimes including cavitating flow. Eur. J. Mech. B Fluids 36, 63–74.

Ducoin, A., Barber, R.B., Wildy, S.J., Codrington, J.D., Baker, A., 2023. Experimental evaluation of the use of embedded fiber bragg gratings to measure steady and unsteady flow-induced marine propeller blade deformation. Ocean Eng. 281, 114889.

Faure, T., Roncin, K., Viaud, B., Simonet, T., Daridon, L., 2022. Flapping wing propulsion: Comparison between discrete vortex method and other models. Phys. Fluids 34 (3).

Gardner, A.D., Jones, A.R., Mulleners, K., Naughton, J.W., Smith, M.J., 2023. Review of rotating wing dynamic stall: Experiments and flow control. Prog. Aerosp. Sci. 137, 100887.

Gordnier, R.E., Chimakurthi, S.K., Cesnik, C.E., Attar, P.J., 2013. High-fidelity aeroelastic computations of a flapping wing with spanwise flexibility. J. Fluids Struct. 40, 86–104.

Hammer, P.R., Garmann, D.J., Visbal, M.R., 2022. Effect of aspect ratio on finite-wing dynamic stall. AIAA J. 60 (12), 6581–6593.

Harwood, C.M., Brucker, K.A., Miguel, F., Young, Y.L., Ceccio, S.L., 2014. Experimental and numerical investigation of ventilation inception and washout mechanisms of a surface-piercing hydrofoil. In: 30th Symposium on Naval Hydrodynamics, Hobart, Tasmania, Australia.

Heathcote, S., Wang, Z., Gursul, I., 2008. Effect of spanwise flexibility on flapping wing propulsion. J. Fluids Struct. 24 (2), 183–199.

Herath, M.T., Phillips, A.W., St. John, N., Brandner, P., Pearce, B., Prusty, G., 2021. Hydrodynamic response of a passive shape-adaptive composite hydrofoil. Mar. Struct. 80, 103084.

Hoffmann, M., Reuss Ramsay, R., Gregorek, G., 1996. Effects of grit roughness and pitch oscillations on the NACA 4415 airfoil. Technical Report, National Renewable Energy Lab.(NREL), Golden, CO (United States); The Ohio ....

Holst, D., Church, B., Wegner, F., Pechlivanoglou, G., Nayeri, C., Paschereit, C., 2019. Experimental analysis of a NACA 0021 airfoil under dynamic angle of attack variation and low Reynolds numbers. J. Eng. Gas Turbines Power 141 (3), 031020.

Janiszewska, J., Ramsay, R.R., Hoffman, M., Gregorek, G., 1996. Effects of grit roughness and pitch oscillations on the LS (1)-0417MOD airfoil. Technical Report, National Renewable Energy Lab.(NREL), Golden, CO (United States).

Jumper, E., Schreck, S., Dimmick, R., 1987. Lift-curve characteristics for an airfoil pitching at constant rate. J. Aircr. 24 (10), 680–687.

Karbasian, H.R., Kim, K.C., 2016. Numerical investigations on flow structure and behavior of vortices in the dynamic stall of an oscillating pitching hydrofoil. Ocean Eng. 127, 200–211.

Kerdraon, P., Horel, B., Bot, P., Letourneur, A., David Le Touzé, D., 2021. High froude number experimental investigation of the 2 DOF behavior of a multihull float in head waves. J. Sail. Technol. 6 (01), 1–20.

Khalifa, N.M., Rezaei, A., Taha, H.E., 2023. On computational simulations of dynamic stall and its three-dimensional nature. Phys. Fluids 35 (10).

Le Fouest, S., Deparday, J., Mulleners, K., 2021. The dynamics and timescales of static stall. J. Fluids Struct. 104, 103304.

McCroskey, W.J., McAlister, K., Carr, L., Pucci, S., Lambert, O., Indergrand, R., 1981. Dynamic stall on advanced airfoil sections. J. Am. Helicopter Soc. 26 (3), 40–50.

Mulleners, K., Raffel, M., 2012. The onset of dynamic stall revisited. Exp. Fluids 52, 779–793.

de Paula, A.A., 2016. The airfoil thickness effects on wavy leading edge phenomena at low Reynolds number regime (Ph.D. thesis). Universidade de São Paulo.

Perali, P., Hauville, F., Leroyer, A., Astolfi, J.-A., Visonneau, M., 2024. Experimental and numerical study of the flow around rigid and flexible hydrofoils for wetted and cavitating flow conditions. J. Fluids Eng. 146 (11).

Pernod, L., Ducoin, A., Le Sourne, H., Astolfi, J.-A., Casari, P., 2019. Experimental and numerical investigation of the fluid-structure interaction on a flexible composite hydrofoil under viscous flows. Ocean Eng. 194, 106647.

Phillips, A.W., Cairns, R., Davis, C., Norman, P., Brandner, P.A., Pearce, B.W., Young, Y.L., 2017. Effect of material design parameters on the forced vibration response of composite hydrofoils in air and in water. In: Fifth International Symposium on Marine Propulsors. pp. 813–822.

Rakotomalala, Q., Rouleau, L., Leblond, C., Abbas, M., Deü, J.-F., 2024. A two-step fluid–structure approach for the vibration analysis of flexible propeller blade. J. Fluids Struct. 126, 104091.

Ramsay, R., Hoffman, M., Gregorek, G., 1995. Effects of grit roughness and pitch oscillations on the S809 airfoil. Technical Report, National Renewable Energy Lab.(NREL), Golden, CO (United States).

Reuss Ramsay, R., Hoffman, M., Gregorek, G., 1996. Effects of grit roughness and pitch oscillations on the S815 airfoil. Technical Report, National Renewable Energy Lab.(NREL), Golden, CO (United States); The Ohio ....

ROBINSON, M., WISSLER, J., 1988. Pitch rate and Reynolds number effects on a pitching rectangular wing. In: 6th Applied Aerodynamics Conference. p. 2577.

Seaver, M., Trickey, S.T., Nichols, J.M., 2006. Strain measurements from FBGs embedded in rotating composite propeller blades. In: Optical Fiber Sensors. Optica Publishing Group, p. ThD2.

Shayanpoor, A.A., Hajivand, A., Moore, M., 2020. Hydroelastic analysis of composite marine propeller basis fluid-structure interaction (FSI). Int. J. Marit. Technol. 13, 51–59.

Simonet, T., Roncin, K., Lapierre, L., Daridon, L., 2020. Étude de l'efficience d'un système de propulsion maritime par foil oscillant souple. In: 17ÈMes JournÉEs de L'Hydrodynamique.

Ullah, A.H., Fabijanic, C., Estevadeordal, J., 2024. Dynamic stall characteristics of unswept pitching wing. Exp. Therm Fluid Sci. 152, 111111.

Visbal, M.R., Garmann, D.J., 2018. Analysis of dynamic stall on a pitching airfoil using high-fidelity large-eddy simulations. AIAA J. 56 (1), 46–63.

Yeager, M., Whittaker, A., Todd, M., Kim, H., Key, C., Gregory, W., 2017. Impact detection and characterization in composite laminates with embedded fiber bragg gratings. Procedia Eng. 188, 156–162.

Young, Y.L., Garg, N., Brandner, P.A., Pearce, B.W., Butler, D., Clarke, D., Phillips, A.W., 2018. Load-dependent bend-twist coupling effects on the steady-state hydroelastic response of composite hydrofoils. Compos. Struct. 189, 398–418.

Young, Y.L., Valles, Z., Di Napoli, I., Montero, F.M., Minerva, L.F., Harwood, C., 2023. Wave effects on the hydroelastic response of a surface-piercing hydrofoil. Part 1. Fully wetted and ventilated flows. J. Fluid Mech. 963, A37.

Zarruk, G.A., Brandner, P.A., Pearce, B.W., Phillips, A.W., 2014. Experimental study of the steady fluid–structure interaction of flexible hydrofoils. J. Fluids Struct. 51, 326–343.

Zhang, X., Schlüter, J.U., 2012. Numerical study of the influence of the Reynolds-number on the lift created by a leading edge vortex. Phys. Fluids 24 (6).